Position Resolution of the ATLAS Electromagnetic Endcap Calorimeter

by

Tayfun Ince
B.Ed. (Physics), Marmara University, Istanbul, Turkey, 1999

A Thesis Submitted in Partial Fulfillment of the
Requirements for the Degree of

MASTER OF SCIENCE

in the Department of Physics and Astronomy

Supervisor: Dr. R. K. Keeler

Abstract

The position reconstruction performance of the Electromagnetic Endcap Calorimeter (EMEC) is assessed in terms of its response to electrons. The electromagnetic and hadronic endcap calorimeter modules of the ATLAS detector are exposed to beams of electrons, pions, and muons in the energy range 6 GeV $\leq E \leq$ 200 GeV at several impact positions in the pseudo-rapidity interval $1.6 \leq |\eta| \leq 1.8$ in a beam test at CERN. The EMEC is a lead-liquid argon sampling calorimeter with a unique accordion structure designed to provide complete hermiticity and excellent energy and position resolution, the attribute on which several physics measurements envisioned at the LHC will depend. Unlike the real ATLAS situation, the beam test setup used a non-pointing geometry in η due to the experimental constraints. Hence, the position resolution of the EMEC is evaluated in the ϕ direction only and found to be at least as good as $\sigma_\phi = (4.36 \pm 0.10)/\sqrt{E(\mathrm{GeV})} \oplus (12.64 \pm 0.82)/E(\mathrm{GeV}) \oplus (0.00 \pm 0.10)$ in milliradians.

Supervisor: Dr. R. K. Keeler, (Department of Physics and Astronomy)

Contents

Abstract ii

Table of Contents iii

List of Figures vi

List of Tables ix

Acknowledgements x

Dedication xi

Glossary of Abbreviations xii

1 Introduction 1

1.1 ATLAS and the LHC 2

1.1.1 The ATLAS coordinate system 8

2 Principles of Electromagnetic Calorimetry 10

2.1 Electromagnetic Interactions 10

2.1.1 Ionization 11

2.1.2 Bremsstrahlung 12

2.1.3 Pair production 12

2.1.4 Photoelectric effect 14

2.1.5 Compton scattering 14
2.2 Electromagnetic Showers 15
2.2.1 Longitudinal development 16
2.2.2 Lateral development 19
2.3 Pions and Muons Traversing Dense Medium 20
2.4 Sampling Calorimetry 21
2.4.1 Liquid argon as the active material 22
2.4.2 Resolution 24

3 The ATLAS Calorimetry 26
3.1 Overview 26
3.2 The Hadronic Endcap Calorimeter 27
3.3 The Electromagnetic Endcap Calorimeter 29
3.3.1 Performance requirements 29
3.3.2 Design 29

4 Beam Test 41
4.1 Experimental Setup 41
4.1.1 The beam test coordinate system 44
4.2 Signal Reconstruction 45

5 Data Selection and Position Reconstruction 47
5.1 Analysis Tools 49
5.2 Stage I – Run Selection 50
5.3 Stage II – Event Selection 53
5.4 Stage III – Clustering 62

6 Results and Systematics 67

6.1 Position Resolution 67
6.2 Corrections 73
6.3 Alternate Clustering Methods 81

7 Conclusions **84**

References **86**

A Beam Test Data Runs **90**

B Theoretical Shower Shape Analysis **92**

C Analytical Calculation of the Position Resolution **95**

D Summary of Position Resolution Results **98**

Partial Copyright License **100**

List of Figures

1.1 Schematic diagram of a proton-proton collision 3
1.2 Feynman diagrams of the Higgs boson production 4
1.3 Higgs decay channels' branching ratios as a function of its mass 4
1.4 Feynman diagram of the Higgs boson decaying into two photons 5
1.5 Geometrical layout of the ATLAS detector 7
1.6 Cut-away view of one endcap cryostat. 8
1.7 Signal significance of the Higgs boson in various decay channels 9

2.1 Energy loss of photons in lead 13
2.2 Schematic diagram of the Compton scattering process 15
2.3 Fractional energy loss of electrons in lead 16
2.4 Schematic diagram of an electron initiated shower 18
2.5 Lateral profile of EM showers 19
2.6 Ionization induced current as a function of time 23
2.7 Ionization signal measured as a function of time 24

3.1 Schematic view of the ATLAS calorimetry system 28
3.2 Schematic view of a cross section of a half EMEC at room temperature . . 30
3.3 Schematic view of an EMEC module 31
3.4 Schematic diagram of the readout electrode structure 32
3.5 High voltage layer of an electrode of the EMEC outer wheel 36

3.6 Layout of the instrumented readout channels of the PS 37
3.7 Layout of the instrumented readout channels of the EMEC Layer 1 38
3.8 Layout of the instrumented readout channels of the EMEC Layer 2 39
3.9 Layout of the instrumented readout channels of the EMEC Layer 3 40

4.1 Schematic view of the general beam test setup 42
4.2 Top view of the beam test cryostat 43

5.1 The MPWC reconstructed x-position of 119 GeV electrons at $z = 0$ 53
5.2 The energy response of the EMEC to a 119 GeV electron beam 55
5.3 The energy response of the EMEC to 119 GeV selected electron events . . . 56
5.4 The comparison of x_{mwpc} and x_{cal} at 148 GeV 58
5.5 The comparison of x_{mwpc} and x_{cal} at 60 GeV 59
5.6 The comparison of y_{mwpc} and y_{cal} at 60 GeV 60
5.7 The comparison of x_{mwpc} and x_{cal} at 60 GeV after the correlation cut . . . 61
5.8 The reconstructed signal distribution of a cell with no energy 63

6.1 The distribution of the difference between ϕ_{mwpc} and ϕ_{cal} 68
6.2 The position resolution in ϕ as a function of beam energy 71
6.3 The position resolution in ϕ as a function of beam impact position 73
6.4 The mean position resolution in ϕ as a function of beam energy 74
6.5 The energy response of 119 GeV electrons as a function of ϕ in cell units . . 75
6.6 The energy response as a function of channel position 77
6.7 The energy response as a function of global time 78
6.8 The corrected mean position resolution in ϕ as a function of beam energy . 79
6.9 The ϕ-resolution as a function of energy power n 80
6.10 Uncorrected mean position difference as a function of impact point 81
6.11 The comparison between fixed and sliding window clustering methods . . . 82

6.12 The comparison between fixed and topological clustering methods 83

A.1 Standard beam impact point positions 90

A.2 Positron shape study impact points 91

List of Tables

3.1 Geometrical dimensions of a readout cell. 34

4.1 Geometrical dimensions of the pre-trigger counters 43

5.1 The information stored in an ATHENA output ROOT file 50

5.2 The information stored in the run statistics database 52

6.1 Weighted mean position resolution results for 6-148 GeV electrons 72

A.1 Electron run numbers at standard impact points 91

A.2 Positron shape study run numbers at 119 GeV 91

B.1 The EMEC material properties. 93

B.2 Dimensions of the active volume of the EMEC outer wheel. 94

B.3 Effective Molière radius and the radiation length of the EMEC 94

C.1 Input parameters of equation C.2 96

C.2 Input parameters of equation C.5 97

D.1 Uncorrected position resolution results from 6 to 30 GeV electrons 98

D.2 Uncorrected position resolution results from 40 and 148 GeV electrons . . . 99

Acknowledgements

My journey in the world of particle physics began about three years ago. I have had the privilege of learning from and working with many great people during this time.

I would like to thank: the ATLAS Liquid Argon EMEC/HEC Collaboration for the unified effort that led to the data analyzed in this work; the UVic Physics and Astronomy department faculty, staff and my fellow graduate student colleagues for making this experience the one to remember in a truly unique environment where every single door is open (literally) at all times; the UVic ATLAS group for sharing their insights and expertise every step of the way; Dr. Charles Picciotto for the second chance he granted which will never be forgotten and I hope this thesis and the contributions I will (wish to) be making to science in the future was worth that second chance; Dr. Ian Bailey and Dominique Fortin for sharing their experience, being good friends, office mates and my oral defense trainers; Tamara Hughes for being an exceptional colleague and a great friend; and Dr. Michel Lefebvre for the patience and time he has invested to answer all my questions (essentially being like my co-supervisor) with an incredible passion and love for science I have never seen before.

And, finally, the Oscar goes to Dr. Richard K. Keeler. I have spent the last two days thinking how to acknowledge the contributions Richard has made to this work, my knowledge of science and a whole lot more. I concluded that the way Richard supervised me cannot be credited in no less than the number of pages in this thesis. His supervision needs to be studied and taught to all faculty at the University of Victoria. I have asked myself many times "am I good enough to deserve the honour of having known and been working with Richard?". Well, the answer has always been and will be "no" which has been one of the driving forces behind my motivation to be a better person and a scientist. Thank you for everything Richard. I could not have made it without you.

Aileme...

Sizlerin sonsuz desteğine layık olmak,

hayatımdaki en büyük hedef olmaya devam edecek.

Glossary of Abbreviations

ADC	Analogue to Digital Converter
ATHENA	ATLAS Main Object Oriented Software Framework
ATLAS	A Toroidal LHC ApparatuS
CERN	European Organization for Nuclear Research
EM	Electromagnetic
EMEC	Electromagnetic Endcap Calorimeter
FCAL	Forward Calorimeter
HEC	Hadronic Endcap Calorimeter
LAr	Liquid Argon
LEP	Large Electron Positron Collider
LHC	Large Hadron Collider
MINUIT	Function Minimization and Error AnalysisTool
MWPC	Multiwire Proportional Chamber
PS	Presampler
QED	Quantum Electrodynamics

ROOT An Object Oriented Data Analysis Software Framework

SM Standard Model

SPS Super Proton Synchrotron

TDC Time to Digital Converter

Chapter 1

Introduction

The Standard Model (SM) [1] [2] [3] is the most experimentally tested theory that incorporates our current understanding of the elementary particles that make up the matter around us and the interactions between these particles. A massive scalar particle known as the Higgs boson is the only remaining particle predicted by the SM that has not yet been discovered. The search for the Higgs boson and the evidence of physics beyond the SM are the highest priorities of particle physics today and the principal reasons for the construction of the Large Hadron Collider (LHC), a new high energy particle collider, and ATLAS, a general purpose detector designed to discover the Higgs.

This thesis studies the position resolution of the electromagnetic calorimeter modules (EMEC) that will be used in the endcap regions of the ATLAS experiment at the LHC. A general overview is given in this introduction of ATLAS and the LHC in order to motivate the measurements and the analysis described in this dissertation. The next chapters will detail the principles of electromagnetic calorimetry, the design of the ATLAS calorimeters and in particular the EMEC, the beam test setup and signal reconstruction, data selection and the position reconstruction, results and systematic errors from the calculation of the

position resolution, and finally some conclusions.

1.1 ATLAS and the LHC

The LHC [4] is under construction in the existing LEP tunnel at CERN near Geneva Switzerland following the unanimous approval of the 19 member states of CERN in December 1994. The primary purpose of the LHC is to determine whether the Higgs boson, predicted by the SM Higgs mechanism for the origin of mass, really exists.

With proton-proton collisions at a center of mass energy of 14 TeV [5], the LHC will be the highest energy accelerator ever built, recreating the conditions that existed in the universe just 10^{-12} seconds after the Big Bang when the temperature was about 10^{16} degrees [6]. The velocity of the protons in the LHC is only 9.69 km/h less than the speed of light at this energy. The production of a Higgs boson is predicted to be very rare and therefore the LHC is also designed to run at very high luminosity[1], L, of 10^{34} cm^{-2}s^{-1} with a bunch crossing time of 25 ns. The total probability that two protons will interact is relatively large, so there are an average 22 events[2] occurring per bunch crossing or 7×10^8 Hz. The rate of interactions can be calculated from $R = L\sigma$ where σ is the cross section of the process. The predicted total production cross section, calculated in leading order, for a Higgs boson of mass 100 GeV is 35.5 pb [7] (1 pb = 10^{-36} cm^2), so the production rate should be 0.355 s^{-1} at full luminosity. The rate that one actually observes the Higgs boson depends on how it decays and how well the decay products of the Higgs can be separated from processes that

[1] Luminosity is the number of particles per unit area per second crossing at the point where the beams meet.

[2] An event, in this case, is defined as an interaction of two protons that produces a detectable signal in ATLAS.

leave similar signals in ATLAS.

Protons are made up of quarks and gluons, constituents known as partons. At high energies, each proton-proton collision may be viewed as collisions of many partons, each carrying a fraction of the proton momentum. Figure 1.1 illustrates a proton proton

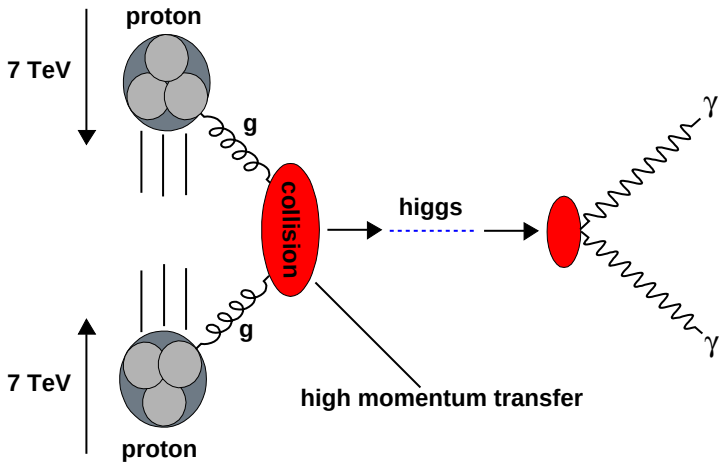

Figure 1.1: Schematic diagram of a proton-proton collision leading to the production of a Higgs boson via the hard interaction between two gluons. The Higgs boson created later decays into two photons.

collision leading to the production of a Higgs boson which later decays, in this illustration, into two photons. The "blobs" in the schematic represent complicated processes that will be discussed below. One complication of a hadron collider, like the LHC, is that the constituent collisions are not in the centre of mass frame but are boosted along the beam direction. A Higgs boson is expected to be mainly produced by the four processes shown in the Feynman diagrams given in figure 1.2. Various decay channels will be used at the LHC to search for the Higgs boson each leaving a particular pattern (signature) in the ATLAS detector. The most probable decay channel depends on the mass of the Higgs as illustrated in figure 1.3 [8].

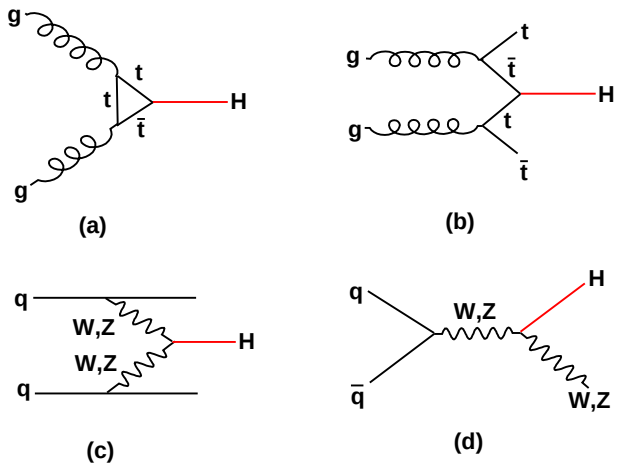

Figure 1.2: Feynman diagrams of the Higgs boson production. (a) gluon-gluon fusion; (b) $t\bar{t}$ fusion; (c) WW and ZZ fusion; (d) W and Z bremsstrahlung.

The Higgs preferentially decays into the gauge bosons (W,Z) and the most massive fermion-

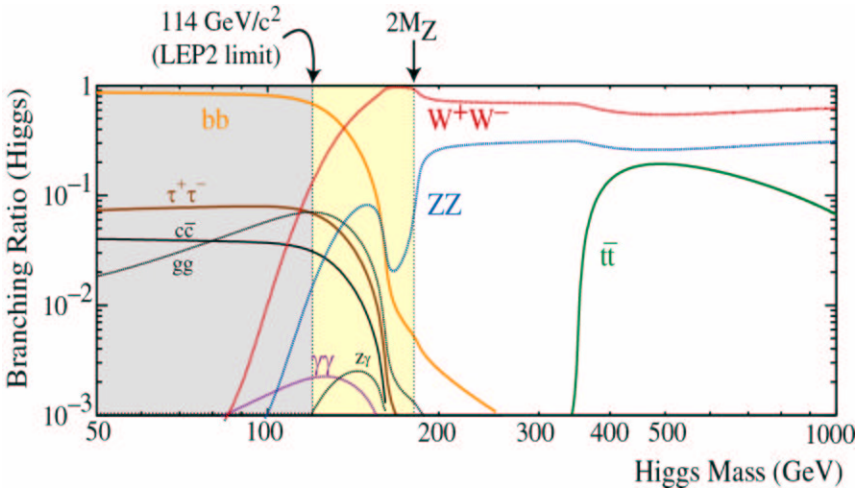

Figure 1.3: Higgs decay channels' branching ratios as a function of its mass. Branching ratio is the probability of occurrence of a particular decay channel. LEP experiments excluded Higgs mass being below 114 GeV at 95% CL through direct searches.

antifermion pair energetically possible. Each of these channels leaves different signature in the ATLAS detector.

ATLAS is a general purpose detector being built to exploit the full physics potential of the LHC. In order to discover the Higgs particle and search for new physics, it must record the energy, momentum and identify the type of particles that are produced in the collisions. A device called a *trigger* selects events that have Higgs like attributes or signatures. An algorithm must then select the particles from these events that are likely to have come from a Higgs and then calculate the mass of the Higgs candidate.

In order to calculate the mass, the momentum and energy of the particles from the decay must be known. Consider a simple two body decay channel $H \to \gamma\gamma$ as an example (see figure 1.4). The mass of the Higgs is reconstructed by

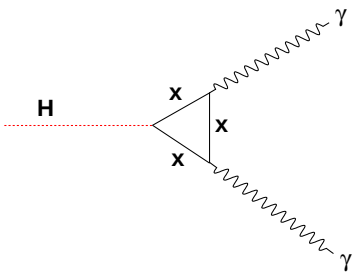

Figure 1.4: Feynman diagram of the Higgs boson decaying into two photons. **x** can be any charged particle, dominated by the top quark, in the SM.

$$\begin{aligned} M_{\mathrm{H}}^2 &= (E_1 + E_2)^2 - \vec{P}_1 \cdot \vec{P}_2 \\ M_{\mathrm{H}}^2 &= (E_1 + E_2)^2 - E_1 E_2 \cos\theta_{12} \end{aligned} \tag{1.1}$$

where M_{H} is the mass of the Higgs, E_i and $\vec{P}_i$ $(i = 1, 2)$ are the energy and the momentum of each photon produced, and θ_{12} is the angle between those two photons. As indicated in figure 1.3, the most likely decay of the Higgs is into W and Z gauge bosons or heavy quarks which will appear in the detector as jets of many lighter mass particles such as pions. For

the more general n body final state, equation 1.1 can be re-written as

$$M_{\mathrm{H}}^2 = \left(\sum_i E_i\right)^2 - \left(\sum_i \vec{P}_i\right)^2 \tag{1.2}$$

where i runs from 1 to n.

Therefore, ATLAS is designed to provide a good energy resolution and a good measurement of the angle which in turn requires good position resolution and the assumption that the photons come from the origin. As can be seen from equation 1.1, both are needed in order to calculate the mass of the Higgs precisely.

ATLAS accomplishes this by using several subdetectors which can be grouped into three main systems that surround the collision origin in layers. The inner detector measures the directions, momentum, and signs of electrically charged particles produced in each proton-proton collision. The calorimetry system measures the energy and the position for charged and neutral particles. As shall be seen in chapter 2, the fractional energy resolution of the calorimetry improves as the incident particle energy increases. Different types of particles leave characteristic signals in the calorimeter and hence the calorimetry system can provide particle identification as well. Finally, the muon spectrometer is for identification and measurement of the momentum of muons specifically. It is on the outside of the detector because high energy muons will generally penetrate the calorimeters. Figure 1.5 shows the geometrical layout of the subcomponents of the ATLAS detector. From the collision center to the exterior of the detector respectively, the inner detector (yellow), the calorimetry system (green and orange) and the muon spectrometer (blue) are clearly visible. One end of the forward region (endcap) of the calorimetry system is displayed in more detail in figure 1.6. The electromagnetic calorimeter in the endcap region of the detector is the

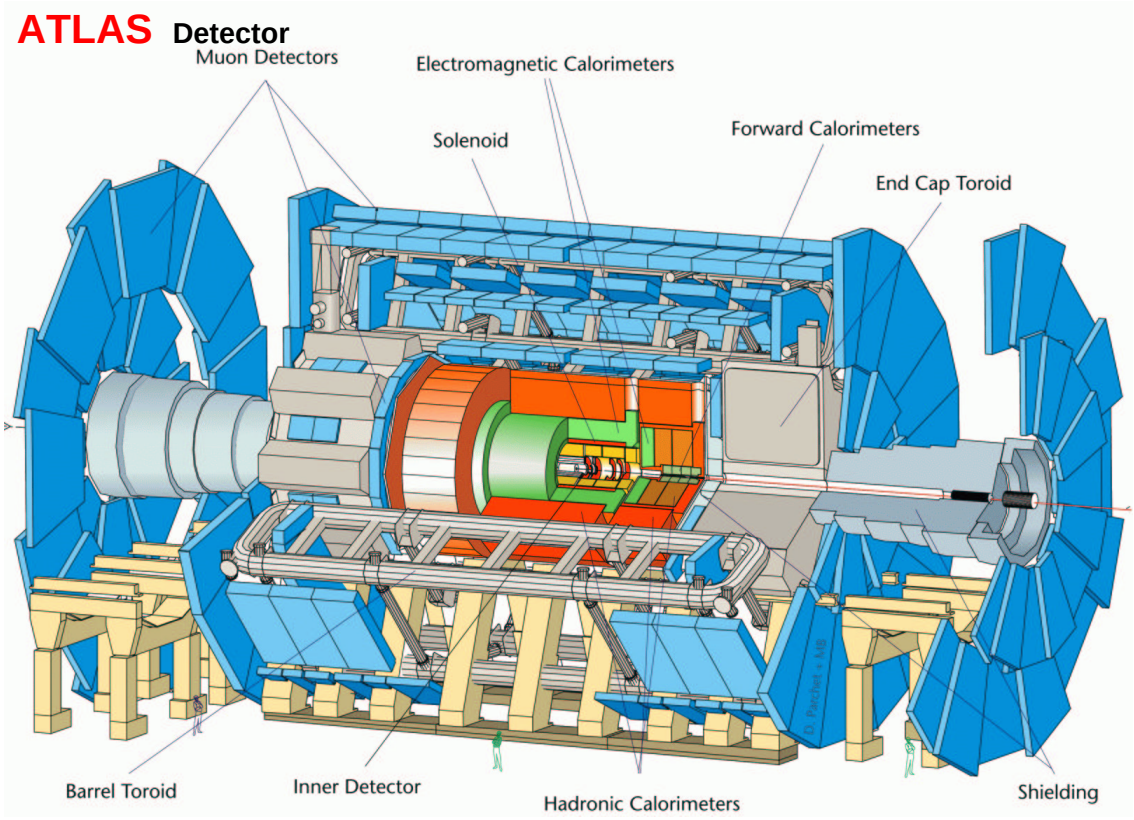

Figure 1.5: Geometrical layout of the ATLAS detector. The detector is about 44 m in length, 22 m in height and weighs 7000 tons.

focus of this thesis and is in front of (closer to the collision center) the hadronic endcap calorimeters.

ATLAS will be capable of discovering the Higgs boson over the mass range of 80 GeV to 1000 GeV (see figure 1.7 which shows the theoretically preferred range of 100 GeV to 200 GeV [9]), although LEP already excluded Higgs mass being below 114 GeV at 95% confidence level. The figure shows the size of the signal divided by the error on the background measurement, a quantity called *signal significance*. A signal significance of 5, i.e. the signal is 5 times bigger than the uncertainty on the background, is considered a solid

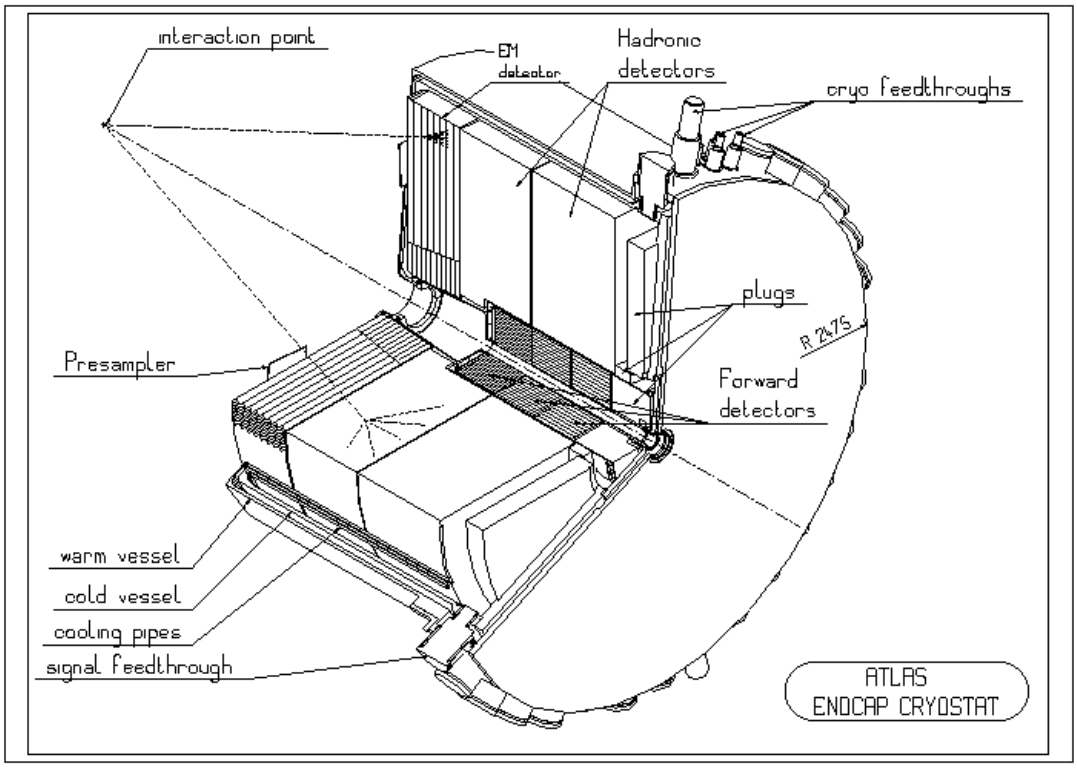

Figure 1.6: Cut-away view of one endcap cryostat.

and reliable criteria for the discovery of a new particle or phenomenon. The figure shows the signal significance for various Higgs signatures as a function of the Higgs mass. The background is from other known processes that produce similar signatures but usually do not form a peak at a particular invariant mass. Other sources of background come from, for example, misidentification of particles and from finite measurement resolution.

1.1.1 The ATLAS coordinate system

The ATLAS coordinate system is a spherical polar coordinate system where positive z direction lie on the beam axis and form a right handed coordinate system with x-axis pointing towards the center of the LHC ring, θ is the polar angle measured from the beam

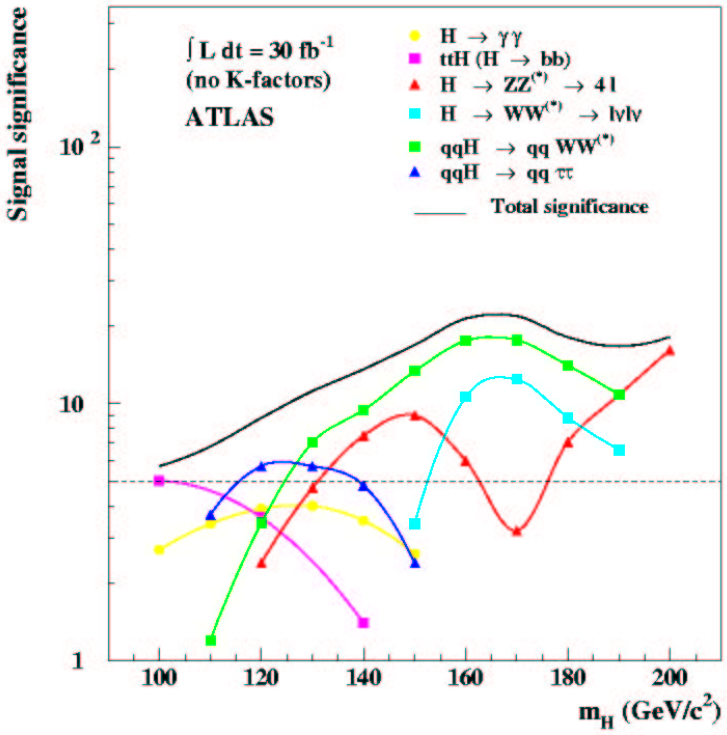

Figure 1.7: Signal significance of the Higgs boson in various decay channels as a function of its mass. Signal significance is defined as the expected number of signal events divided by the square root of the expected number of background events (i.e. $S/\sqrt{B}$). Poisson statistics is used to determine the signal significance, when $S + B$ is less than 25.

axis and ϕ is the azimuthal angle. In practice, the polar angle is expressed in terms of pseudorapidity[3] which simplifies the calculation of cross section and other observables for the case when the hard scatter centre of mass moves in the lab frame. These coordinates will be used to relate the orientation of the ATLAS calorimeter modules to the coordinates used in the beam test.

[3]Pseudorapidity is defined as $\eta = -\ln\left(\tan\frac{\theta}{2}\right)$.

Chapter 2

Principles of Electromagnetic Calorimetry

Particles interact with matter and lose energy through electromagnetic and strong interactions depending on the nature of the particle.

In this chapter, the physics behind the electromagnetic shower phenomenon is discussed with an emphasis on understanding the lead-liquid argon electromagnetic calorimetry system used in the ATLAS detector.

2.1 Electromagnetic Interactions

Charged particles and photons interact with matter through the electromagnetic (EM) force. Therefore, for the purpose of this study, the interactions of electrons, positrons and photons are of primary interest.

All charged particles lose energy in matter via ionization and excitation of the atoms in the medium. Electrons and positrons also radiate energy as photons when decelerated because of interactions with the medium. Photons interact with matter through e^+e^- pair production, photoelectric effect and scattering processes such as Compton scattering.

The following sections describe these interactions. First, the interactions of electrons and positrons with matter and, then, the interactions of photons with matter are discussed.

2.1.1 Ionization

Generally, atoms and molecules are electrically neutral[1]. However, if there is sufficient energy available, atoms or molecules can lose electrons and acquire a net electrical charge. This process is known as ionization. If the atom is excited to a higher energy but an electron is not liberated, the process is called excitation. Charged particles and photons traversing a medium may transfer energy to the constituent atoms via ionization or excitation resulting in the loss of energy of the incident particle and the generation, in the case of ionization, of ion pairs (positive ion and electron). The number of such pairs produced is proportional to the energy lost by the incident particle.

The energy loss via ionization and excitation is parametrized by the Bethe-Bloch [10] equation[2];

$$-\frac{dE}{dx} = 4\pi N_0 r_e^2 m_e c^2 z^2 \frac{Z}{A}\frac{1}{\beta^2}\left[\frac{1}{2}\ln\left(\frac{2m_e c^2\beta^2 T_{\max}}{I(1-\beta^2)}\right) - \beta^2 - \frac{\delta}{2}\right] \tag{2.1}$$

where $\frac{dE}{dx}$ is the mean energy deposition per unit path length (i.e. x is in mass per unit area), m_e and r_e are the mass and classical radius of the electron, z and β are the charge (in units of $e = 1.6022 \times 10^{-19}$C) and the velocity ($\beta = v/c$) of the particle, N_0 is Avogadro's number, Z and A are the atomic and the mass numbers of the atoms of the medium, I is the mean ionization potential which is approximately $10Z$ eV, $T_{\max}$ is the maximum kinetic energy transferable to a free electron in a single collision and δ is the density effect

[1] The number of electrons is exactly equal to the number of protons

[2] This is usually referred to as ionization energy loss and this convention will be followed in this thesis.

correction to ionization energy loss.

2.1.2 Bremsstrahlung

A charged particle traversing a medium scatters in the electric fields generated by the atomic electrons and nuclei and undergoes a small change in direction (the process known as Coulomb scattering) and hence is decelerated. Therefore, it radiates. The radiation produced in this process is called bremsstrahlung[3]. Because the electrons and the positrons are the lightest particles, they radiate the most. Bremsstrahlung is the primary source of energy loss by high-energy electrons, and has a continuous energy spectrum which falls off as $\frac{1}{E}$, where E is the energy of the incident particle [11]. The total radiation loss of an electron of energy E traversing a thickness dx can be described by

$$\left(\frac{dE}{dx}\right)_{\text{rad}} = -\frac{E}{X_0} \tag{2.2}$$

where X_0 is called the *radiation length* (in mass per unit area) and is defined as the distance over which an incident electron energy is reduced by a factor of $1/e$ (i.e. 0.36) due to bremsstrahlung radiation only (see equation 2.8 given later in this chapter for a formula for X_0 that depends on the properties of the medium).

2.1.3 Pair production

Pair production is the formation of an electron and a positron from a photon traveling through matter. The electron and the positron lose energy via ionization. The positron can also annihilate with an electron in the medium into two or more photons. Pair production is by far the principal process in which high energy photons are absorbed in matter (see

[3]German for breaking radiation

figure 2.1) and occurs only at energies greater than twice the electron rest mass, i.e. 1.022 MeV. The attenuation[4] of a beam of photons of intensity I can be expressed as [12]

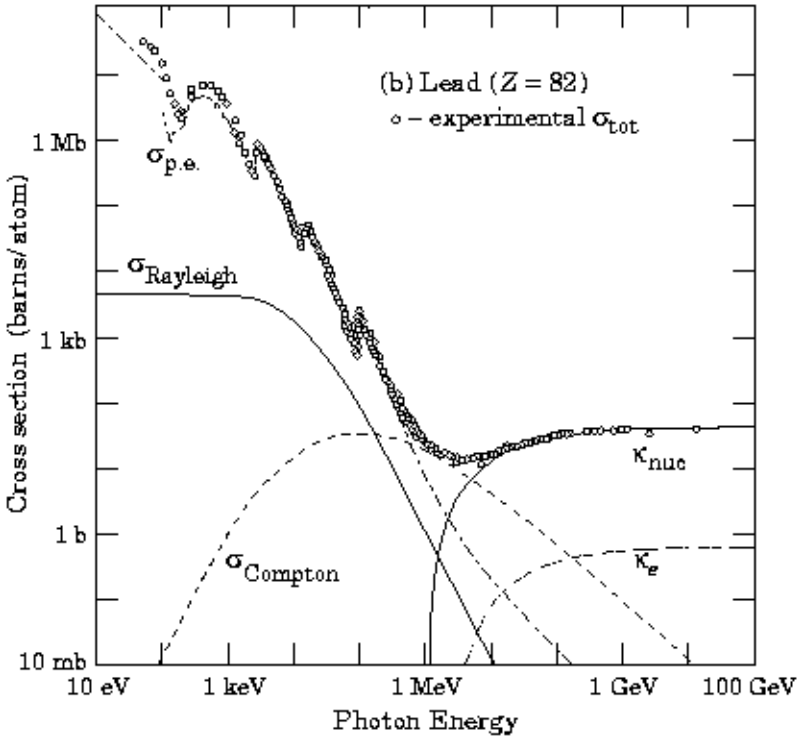

Figure 2.1: The cross sections of photon energy loss mechanisms as a function of energy in lead. $\sigma_{\mathrm{p.e}}$ is for the photoelectric effect, $\sigma_{\mathrm{Rayleigh}}$ is for the Rayleigh scattering, $\sigma_{\mathrm{Compton}}$ is for the Compton scattering, κ_{nuc} is for the pair production due to the nuclear field and κ_{e} is for the pair production due to the electron field.

$$I = I_0 e^{-\mu x} \tag{2.3}$$

where x is the thickness of the medium (in mass per unit area) and μ is the mass absorption coefficient which is related to the cross sections of photon interactions (i.e. pair production, photoelectric effect, Compton scattering, etc.) by

$$\mu = \frac{N_0}{A} \sum_i \sigma_i \tag{2.4}$$

[4]the decrease in intensity as a result of absorption

where σ_i is the cross section of the i^{th} process. The pair production cross section is given by

$$\sigma_{\text{pair}} = \frac{7}{9}\frac{A}{N_0}\frac{1}{X_0} \tag{2.5}$$

where X_0 is the same radiation length contained in equation 2.2 and 2.8.

2.1.4 Photoelectric effect

The photoelectric effect is the process in which an electron is emitted or ejected from an atom in response to the total absorption of an incident photon. Since a free electron cannot absorb a photon and also conserve momentum, the photoelectric effect can only occur on bound atomic electrons with the nucleus absorbing the recoil momentum. At low energies (less than a few hundred keV), this is the dominant energy loss mechanism for photons (see figure 2.1).

2.1.5 Compton scattering

The scattering of photons from an atomic electron (or nucleus) is called *Compton scattering*. It is the most likely interaction to take place for photons in the energy range between 500 keV and 6 MeV in lead (see figure 2.1).

Figure 2.2 shows this scattering process. The relationship between the energies and the scattering angles of the electron (ϕ) and the photon (θ) can be derived, by applying the energy and momentum conservation, as [13]

$$\begin{aligned} E_{\gamma'} &= \frac{E_\gamma}{1+\xi(1-\cos\theta)} \quad , \\ \cot\phi &= (1+\xi)\tan\frac{\theta}{2} \quad , \end{aligned} \tag{2.6}$$

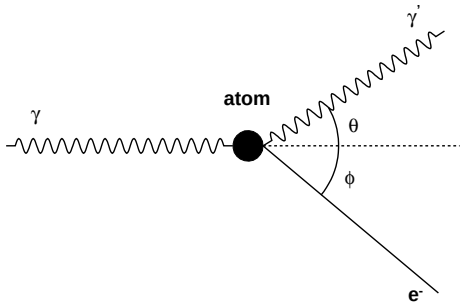

Figure 2.2: Schematic diagram of the Compton scattering process where γ , $\gamma^{'}$ and e^{-} represent the incident photon, the scattered photon and the scattered electron, respectively.

where E_{γ} and $E_{\gamma'}$ are the energy of incident and the scattered photons respectively and ξ is the incident photon energy in units of the electron rest mass, i.e $\xi = E_{\gamma}/m_{\mathrm{e}}c^2$.

2.2 Electromagnetic Showers

EM interactions are the best understood energy-loss mechanisms in high energy physics and in principle can be calculated by Quantum Electrodynamics (QED). Figure 2.3 show the typical EM processes which electrons and/or positrons undergo in lead depending on their energies. At energies above 1 GeV, an electron (or positron) loses its energy almost entirely via bremsstrahlung. The radiated photon from this process will then most likely produce an $e^{-}e^{+}$ pair as a result of the interaction with the EM field of an atomic nucleus or an atomic electron within the medium. Both the electron and positron of the pair may emit a photon if they have sufficient (above 10 MeV) energy. It is through a succession of these mechanisms that a cascade of particles is produced that is known as an *electromagnetic shower.*

As the shower develops, the number of cascade particles will increase exponentially

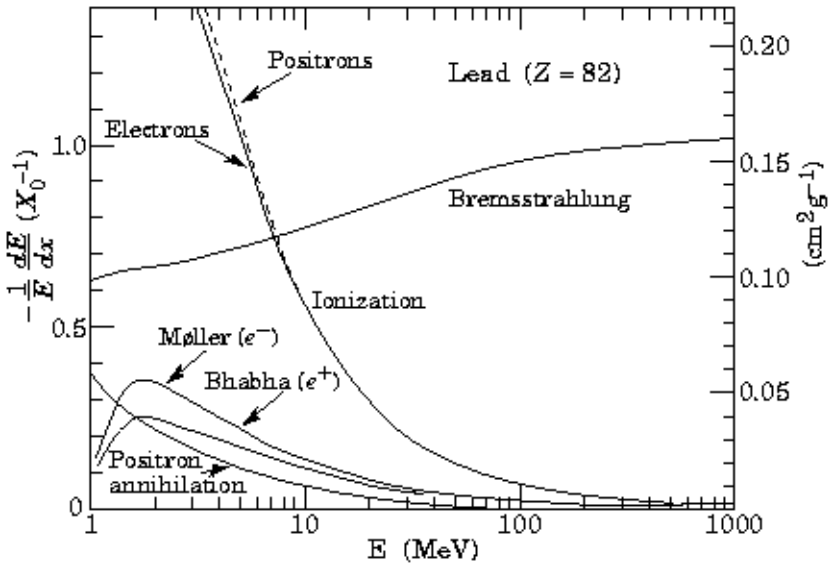

Figure 2.3: Fractional energy loss per radiation length in lead as a function of electron or positron energy. This figure is taken from [10].

until the energy of the shower particles is reduced to the regime where the dissipation of energy via ionization and excitation become dominant. From this point on, the shower dissipates gradually through ionization losses for electrons, by Compton scattering and photoelectric effect for photons.

The energy at which the energy loss via bremsstrahlung equals to the energy loss via ionization is called the *critical energy*, ϵ_c and is expressed as [14]

$$\epsilon_c \cong \frac{800 \text{ MeV}}{Z + 1.2} \quad . \tag{2.7}$$

For example, the critical energy for electrons in lead is 9.6 MeV.

2.2.1 Longitudinal development

The EM shower development depends on the density of electrons in the medium, which is proportional to the atomic number Z of the material. It is possible to characterize

the development of an EM shower in a material-independent way. For the longitudinal development, the radiation length, X_0, is generally used for this purpose and is given by [10]

$$X_0 = \frac{716.4A}{Z(Z+1)\ln(287/\sqrt{Z})} \ \frac{\mathrm{g}}{\mathrm{cm}^2} \ \ (\mathrm{Z} > 4) \tag{2.8}$$

for an element of atomic number Z and atomic mass A given in grams per mole. The radiation length of a mixture or a compound may also be found using the following formula;

$$\frac{1}{X_0} = \sum \frac{w_i}{X_{0i}} \tag{2.9}$$

where w_i and X_{0i} are the fraction by weight and the radiation length for the i^{th} material in the compound or the mixture. The radiation lengths for lead (Pb), copper (Cu) and liquid-argon (LAr) are 0.56 cm, 1.43 cm and 14.0 cm, respectively [10].

Due to the extreme complexity of the mathematical description of an EM shower using QED, several simplifications have been made in order to approximately describe the longitudinal development. For example, a simplified cascade model (illustrated in figure 2.4) is given by Heitler [15] with the following postulates;

- each electron with $E > \epsilon_{\mathrm{c}}$ propagates 1 radiation length and radiates a photon with $E/2$ of its energy,
- each photon with $E > \epsilon_{\mathrm{c}}$ travels 1 radiation length and pair produces an $e^- e^+$ with each of the particles having $E/2$ of the photon's energy,
- electrons with $E < \epsilon_{\mathrm{c}}$ lose their remaining energy to ionization and excitation,
- neglect ionization loss for $E > \epsilon_{\mathrm{c}}$.

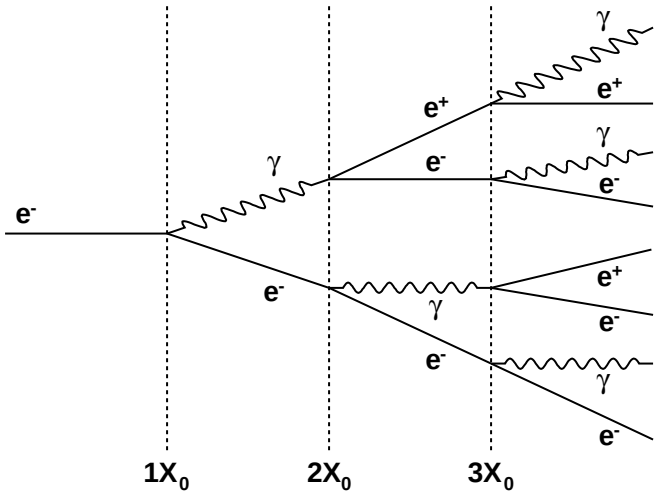

Figure 2.4: Schematic diagram of an electron initiated shower according to the simplified cascade model by Heitler.

Using this model, one can make a number of predictions about EM showers. For example, the total number, N, of the cascade particles after t radiation lengths is approximately $N(t) \cong 2^t = e^{t \ln 2}$. The average energy of a cascade particle at depth t is $E(t) \cong E_0/2^t$ where E_0 is the energy of an incident particle. The maximum number of particles in a shower is reached at $E(t) \cong \epsilon_c$, and the depth at which this occurs is $t_{\max} = \ln(E_0/\epsilon_c)/\ln 2$. Hence, the maximum number, $N_{\max}$, of particles is given by $N_{\max} = e^{t_{\max} \ln 2} = E_0/\epsilon_c$. In addition, there are approximately equal numbers of electrons, positrons and photons in the cascade.

However, in reality, the majority of the bremsstrahlung photons produced in an EM shower have very low energies and are more likely to produce electrons than e^-e^+ pairs through Compton scattering and the photoelectric effect as they are absorbed by the medium. Therefore, there are considerably more electrons than positrons (only produced

via pair creation) in the shower.

2.2.2 Lateral development

The lateral spread of EM showers is mainly due to the multiple Coulomb scattering of electrons and positrons, but photons and electrons which are created via Compton scattering and photoelectric effect also will contribute considerably to the spread. In addition, bremsstrahlung photons which travel away from the shower axis (i.e. direction of the incident particle that initiates the shower) have a non-negligible effect as well, depending on the angle of their direction with respect to the shower axis. Figure 2.5 illustrates the typical of the transverse profile of an EM shower. Note that there is a core region with a long tail.

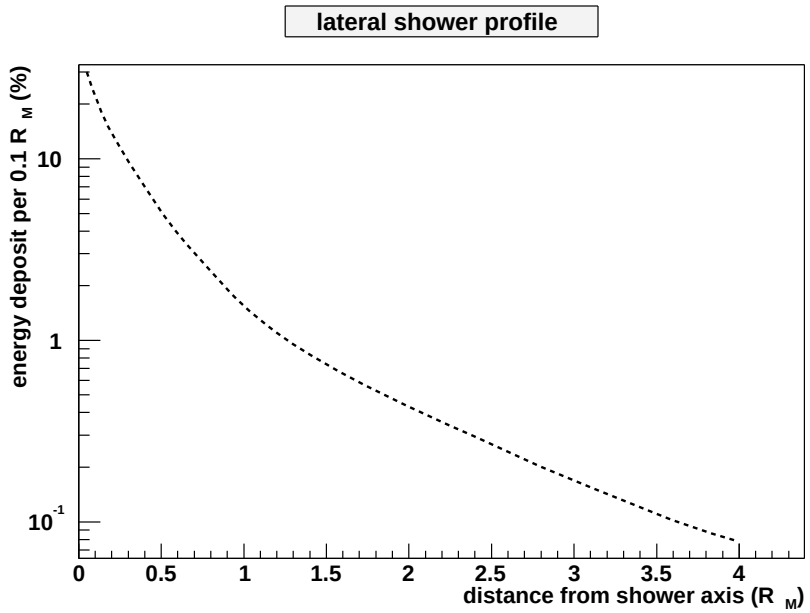

Figure 2.5: Sketch of the lateral profile of the deposited energy by 10 GeV EM showers in lead. This figure is redrawn from [11].

In a similar way to the longitudinal development, the lateral development of an EM shower can also be described in a material-independent way by using the *Molière radius*,

R_{M}. It is defined to be the radius of the lateral spread of electrons of energy ϵ_{c} after traveling 1 radiation length [16], and is formulated as

$$R_{\mathrm{M}} = \frac{21.2 \text{ MeV}}{\epsilon_{\mathrm{c}}} X_0 \cong 7 \frac{A}{Z} \frac{\mathrm{g}}{\mathrm{cm}^2} \tag{2.10}$$

where the scaling factor 21.2 MeV is calculated from $m_{\mathrm{e}}c^2\sqrt{4\pi/\alpha}$. The Molière radii of a mixtures or a compound of different materials can be calculated in a similar way as the radiation length by

$$\frac{1}{R_{\mathrm{M}}} = \sum \frac{w_i}{R_{\mathrm{Mi}}} = \frac{1}{21.2 \text{ MeV}} \sum \frac{w_i \epsilon_{\mathrm{ci}}}{X_{0i}} \tag{2.11}$$

where R_{Mi} is the Molière radii of the ith component of the compound (or the mixture).

On average, 95% of the energy of an EM shower is contained laterally in a cylinder with radius $2R_{\mathrm{M}}$. The scaling with R_{M} fails beyond $3.5R_{\mathrm{M}}$ (i.e. $\approx$ 99% containment).

2.3 Pions and Muons Traversing Dense Medium

Hadrons (baryons and mesons, e.g. pions) can interact with the nucleus of the medium via the strong force producing a number of charged and neutral hadrons. The charged secondary hadrons (π^+, π^-, p, etc.) will then lose energy through ionization and further strong (nuclear) interactions. On the other hand, the neutral hadrons (π^0, η) produced will decay electromagnetically into two photons almost exclusively. Hence, hadronic showers produced through a succession of these mechanisms will have a hadronic component and an electromagnetic component. The physics that governs the purely hadronic component is far more complex than that of EM showers due to the large number of reactions possible between hadrons and the nuclear matter of the medium (more than 300 processes with cross sections 0.1% and more) that contribute to the energy lose. The size of the hadronic shower

is given by the nuclear interaction length, λ_{int}, defined as the mean length of medium traversed by the hadron before interacting with a nucleus of the medium. The nuclear interaction lengths for Pb, Cu and LAr are 17.09 cm ($\sim 30X_0$), 15.06 cm ($\sim 10X_0$) and 83.95 cm ($\sim 6X_0$) [10]. Therefore, the longitudinal depth of a hadronic shower is much ($\sim$ an order of magnitude) larger than that of an EM shower. This also holds true for the lateral spread.

Muons interact with the medium very differently compared to electrons and pions. The critical energy, ϵ_c, of muons is about 40000 times larger than that of electrons since ϵ_c is proportional to the square of the particle mass. Hence, the primary energy loss mechanism for muons is ionization up to very high energies. The energy loss via ionization is small (1-2 MeV g^{-1} cm^2 [11]), so high energy muons travel many times further in the medium than electrons and pions of the same energy.

2.4 Sampling Calorimetry

A calorimeter is an instrument used to measure the energy of the shower and thus, of the incident particle. Calorimeters also offer the ability to detect and measure the energy of neutral particles, unlike magnetic spectrometers that use techniques in which particle momentum is measured by the amount a particle is deflected in a magnetic field and hence are only useful for charged particles. Moreover, the fractional energy resolution provided by calorimeters improves with increasing energy, in contrast with magnetic spectrometers where the resolution degrades with increasing energy. Therefore, calorimeters are the detection devices of choice as particle colliders achieve higher energies.

Calorimeters can be sorted into two fundamental classes: total absorption (homogeneous) and sampling (heterogeneous). Only, sampling calorimetry will be discussed further as this is the type used in ATLAS.

Sampling calorimeters are designed to take many sample measurements of the shower throughout its development. A sampling calorimeter consists of alternate layers of dense absorber material to increase the probability of interactions and make the calorimeter more compact and active material to sample energy loss. In the first generation (to be referred to as conventional) of sampling calorimeters in particle physics, the orientation of these alternate layers was perpendicular to the direction of particles to be detected. Other orientations that offer considerable advantages in terms of detector hermiticity, readout, granularity, etc, have been designed, such as the EMEC with an accordion geometry. The EMEC accordion geometry will be further discussed in Chapter 3. Absorbers used in sampling calorimeters are typically lead, copper and iron depending on the desired radiation or interaction length. Metal-scintillator sandwich, metal-liquid argon ionization chamber and metal-gaseous proportional wire chambers are commonly used types of sampling calorimeters [15]. LAr ionization calorimetry will be the focus of descriptions that follow, since all of the endcap calorimetry in ATLAS makes use of this technique.

2.4.1 Liquid argon as the active material

A LAr calorimeter is made up of a series of metal plates immersed in liquid argon. Ionization electrons produced in the LAr gaps move under the influence of an externally applied electric field. The motion of the electrons induces currents on the plates which can be measured using electronics. Figure 2.6 shows a sketch of the triangular waveform of an

ionization induced current. The collected charge is quite small, since there is no charge multiplication, so a preamplifier and associated signal shaping electronics are needed to amplify the current pulse. The typical shape of the resulting ionization signal in ATLAS is illustrated in figure 2.7.

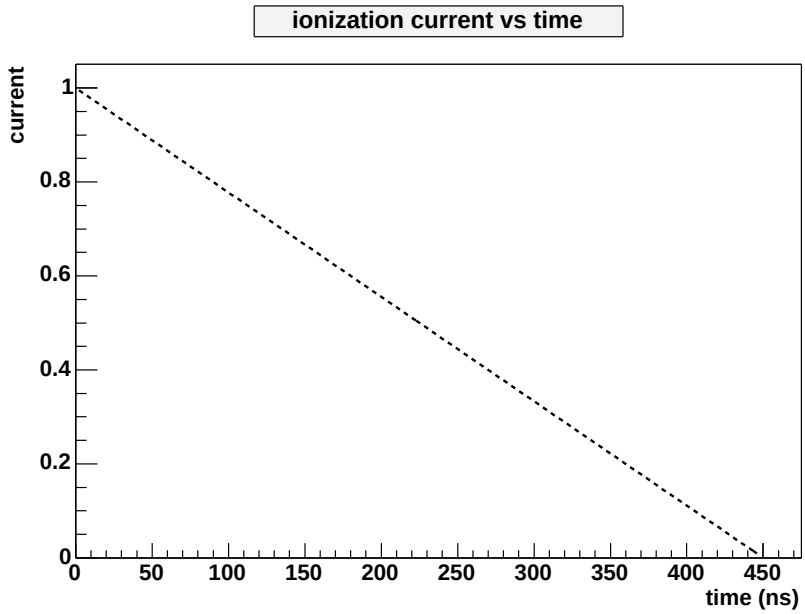

Figure 2.6: Ionization induced current (normalized) as a function of time.

LAr's relatively high electron mobility is one of the main reasons for its wide usage in calorimetry, and since argon is a noble gas, it does not capture free electrons (i.e. no signal loss) if it is absolutely pure. A purity of 1 ppm (parts per million) O_2 equivalent is sufficient for practical purposes. The number of charges collected (i.e. unit gain) at the plates is equal to the number of ion pairs produced and, hence, this makes it easy to calibrate the calorimeter. LAr is also radiation hard which is extremely important because of the high radiation level in the calorimeters of high-energy physics experiments. Finally, having

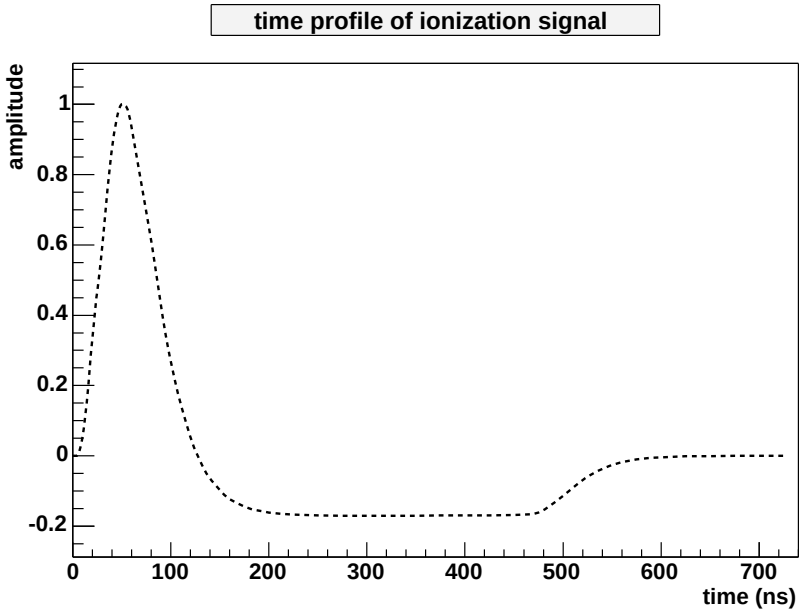

Figure 2.7: Ionization signal measured as a function of time. The vertical axis shows the signal amplitude (normalized). This figure is drawn using table 5 in [17].

an active material in liquid form allows for easy adoption to the necessary geometry while still allowing direct electronic readout.

2.4.2 Resolution

The number of shower particles N in an EM shower is proportional to the energy of the incident particle (see section 2.2.1), and N has a Poisson distribution with variance $\sqrt{N}$. Therefore, the energy resolution, $\sigma(E)/E$, of a calorimeter (to first order) is inversely proportional to the square root of the measured energy. That is

$$\frac{\sigma(E)}{E} \propto \frac{\sqrt{N}}{N} = \frac{1}{\sqrt{N}} \propto \frac{1}{\sqrt{E}} \quad .$$

The energy resolution of an EM sampling calorimeter can, hence, be expressed as the sum of three terms added in quadrature;

$$\frac{\sigma(E)}{E} = \frac{a}{\sqrt{E}} \oplus \frac{b}{E} \oplus c \tag{2.12}$$

where a is the sampling term coefficient which depends on the intrinsic fluctuations of the shower and the sampling fluctuations, b is the coefficient of a term proportional to the electronic noise, and c is the constant term due to the mechanical imperfections of the calorimeter and incomplete shower containment.

Chapter 3

The ATLAS Calorimetry

The ATLAS calorimetry system will play a crucial role in achieving the goals that have driven the design of the detector and the LHC in general. In this chapter, a brief overview of the ATLAS calorimetry is presented with a description of the two detectors that will be used in this thesis; the hadronic endcap calorimeter (HEC), followed by a more detailed focus on the design and performance requirements of the EMEC.

3.1 Overview

The ATLAS calorimeters are designed to provide precision measurements of the energy and the position of electrons, positrons and photons as well as the energy and the direction of jets and missing transverse energy in the very high luminosity (10^{34} cm^{-2}s^{-1}) environment of the LHC [18]. The LHC will have a bunch crossing time of 25 ns with an average 22 events (or 7×10^8 Hz) occurring per bunch crossing. High event rates create two problems: high radiation and event pile-up. In order to withstand the high radiation, radiation resistant materials such as lead, copper and liquid argon are used when possible in the construction of the calorimeters. Pile-up is the superposition of signals which in this case may come

from the same beam crossing or beam crossings nearby in time. In order to limit the effects of pile-up, the signal is shaped so that it is as short as possible. This also gives the added possibility of fast readout. In ATLAS, the duration of the signal is approximately 450 ns, the time it takes an ionization electron to travel from one readout electrode to the next. An electronic circuit shapes the signal to achieve a 50 ns peaking time (see figure 2.7). This type of shaping reduces the signal to electronic noise ratio and, hence, there is a limit on how much the peaking time can be reduced without compromising the quality of the energy and position measurement made using the calorimeters.

There are two different types of calorimeter technology used in ATLAS: liquid argon calorimetry and scintillating tile calorimetry. The LAr sampling calorimetry is chosen for all of the EM calorimeters (barrel and endcap) as well as the HEC and the forward calorimeter (FCAL). A brief discussion on sampling calorimetry, in particular LAr calorimetry was presented in Chapter 2. The tile calorimetry is used only for the barrel hadronic calorimeter. Design details of the calorimeters can be found in the technical design reports [19] and [20]. A three dimensional cut-away view of the calorimetry system is presented in Figure 3.1. The subject of this thesis is the EMEC, but some information from the HEC will also be used.

3.2 The Hadronic Endcap Calorimeter

The HEC, a conventional LAr sampling calorimeter with copper (Cu) plate absorbers oriented perpendicular to the beam axis, is designed to cover hadronic showers in the pseudo-rapidity region in the range $1.5 \leq |\eta| \leq 3.2$ with a total thickness of 1858 mm ($\sim$ 10 nuclear

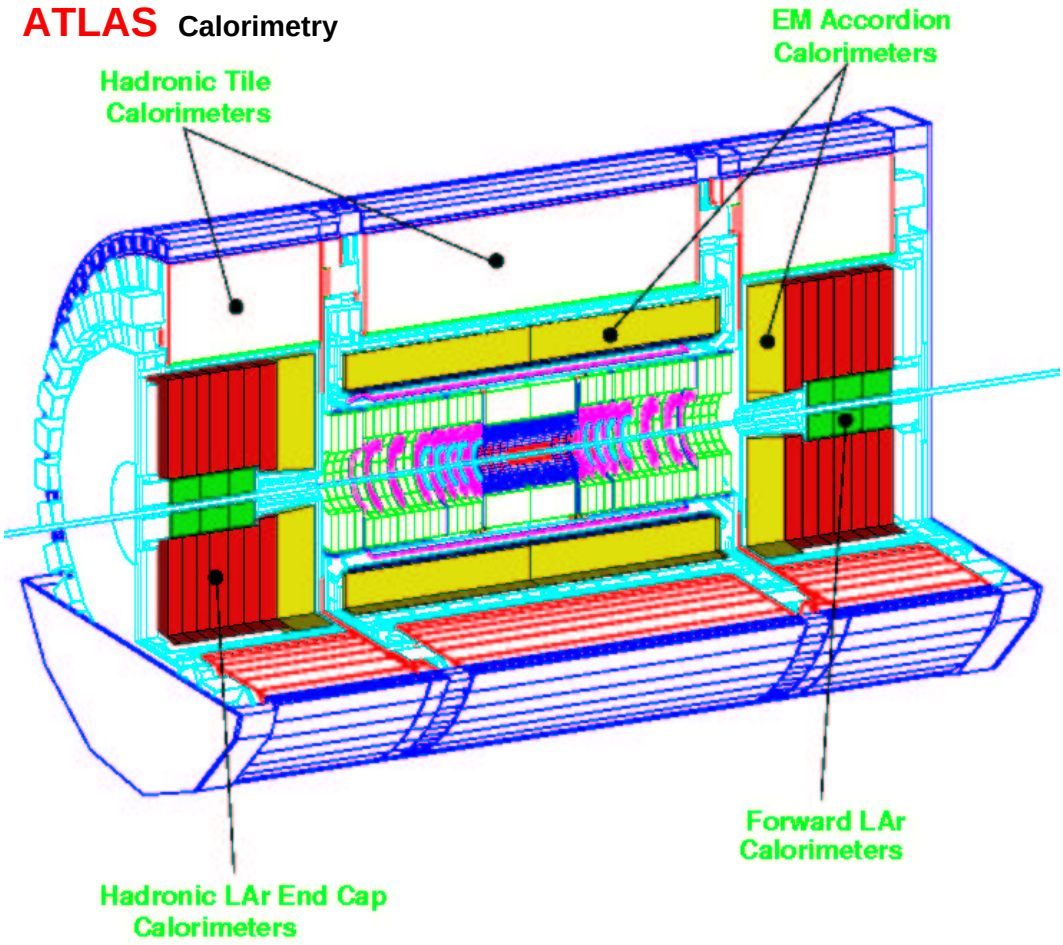

Figure 3.1: Schematic view of the ATLAS calorimetry system. The system is about 13 m in length and 8 m in radius.

interaction lengths) and a radius of 2090 mm.

The HEC wheels are located behind the EMEC wheels in each of the endcap cryostats at both ends of the ATLAS detector. The HEC consists of two wheels (HEC1 and HEC2) each made of 32 pie-shaped identical modules. HEC1 has 25 mm thick copper plates and is divided into two readout depths (front and back) with 8×8.5 mm LAr gaps and 16×8.5 mm LAr gaps respectively. HEC2 has two readout segments (front and back)

both with 8×8.5 mm LAr gaps and 50 mm thick copper plates.

3.3 The Electromagnetic Endcap Calorimeter

The EMEC is a Pb-LAr sampling calorimeter with an accordion geometry unique to ATLAS and is designed to meet the stringent requirements needed in order to accomplish the physics measurements envisioned at the LHC.

3.3.1 Performance requirements

Many important physics processes impose challenging requirements on the EM calorimetry at the LHC [21]. For example, in order to detect the many different signatures of the Higgs, the EM calorimeter must be capable of identifying and reconstructing electrons and photons over an energy range from 1 GeV up to 5 TeV. Excellent energy resolution ($a \leq 10\%\sqrt{\text{GeV}}$ and $c \leq 1\%$ in equation 2.12) over the energy range 10 GeV to 300 GeV along with a very good resolution (approximately 7 mrad$\sqrt{\text{GeV}}$) on the measurement of the shower position is required to be able separate electrons and photons from jets. Finally, good hermiticity and pseudorapidity coverage with the best possible granularity (not coarser than $\Delta\eta \times \Delta\phi = 0.03 \times 0.03$ in radians) also is necessary for fast signal response time and low noise to achieve the physics requirements.

3.3.2 Design

The two EMEC wheels are located about 3.6 m from the interaction point [19] (see Figure 3.1), and cover the pseudorapidity range $1.375 \leq |\eta| \leq 3.2$. Each EMEC is, at 20 ℃ (-196 ℃), 632 mm (630 mm) thick and has an external radius of 2077 mm (2067 mm) as shown in Figure 3.2.

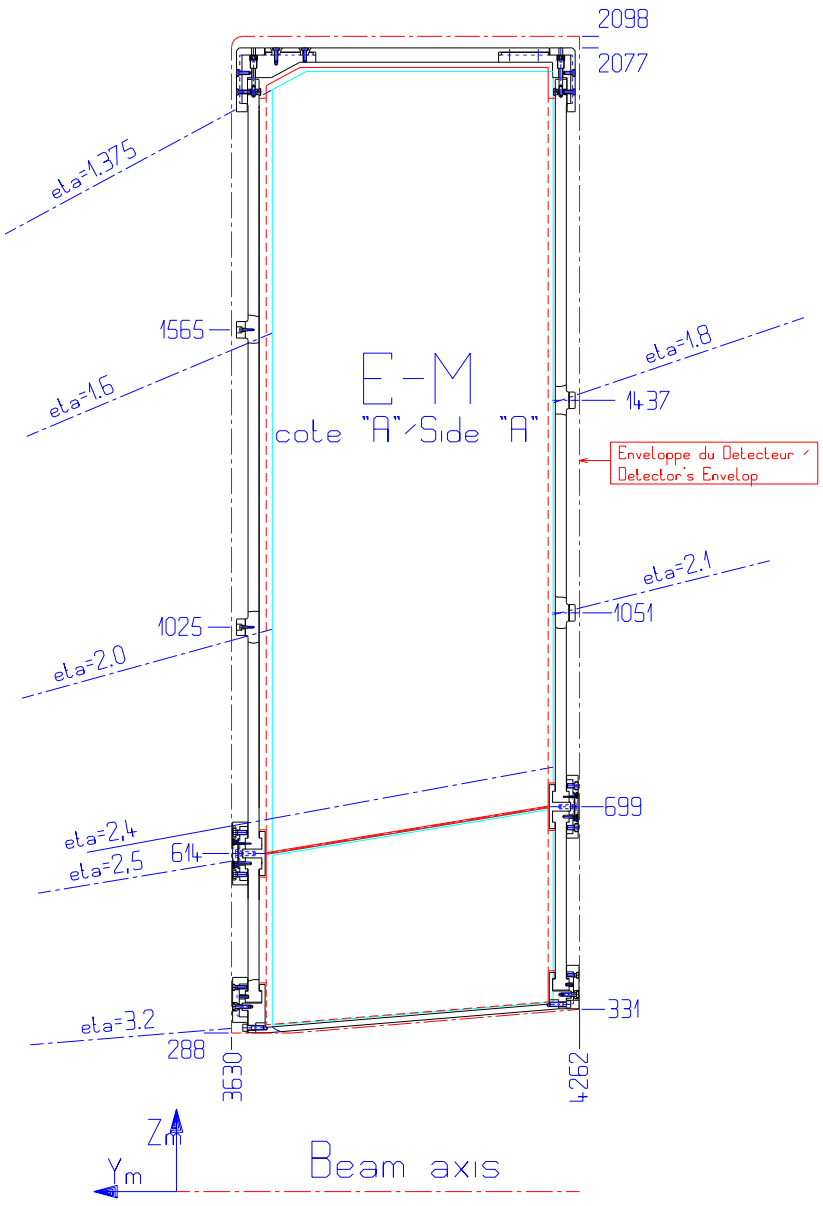

Figure 3.2: Schematic view of a cross section of a half EMEC at room temperature. Note that 3630 mm is the initial design value only.

Each EMEC is made-up of eight pie-shaped modules and consists of lead absorbers bent into a zig-zag (accordion) shape interleaved with electrodes (also accordion shape) oriented parallel to the incident particle direction. The gaps between the electrodes and

absorbers are filled with LAr. The absorber plates are arranged radially with the waves running parallel to the beam axis (see figure 3.3), thereby ensuring a full ϕ symmetric

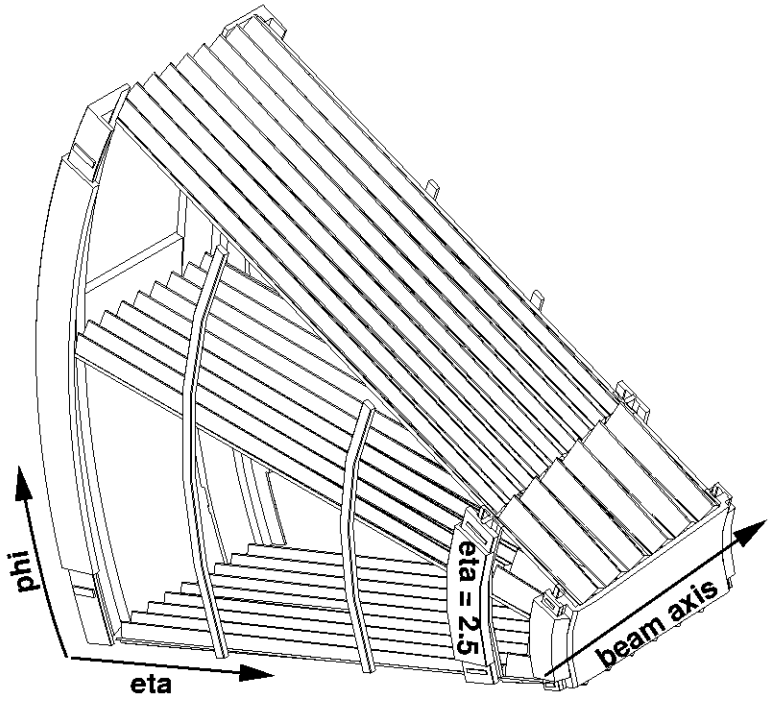

Figure 3.3: Schematic view of an EMEC module. Only 3 absorbers are represented.

geometry which is hermetic (i.e. there are no cracks in ϕ that particles could get through). As the LAr gap naturally increases with radius, it is necessary to adjust the wave height and the folding angle to keep the combined thickness of LAr and absorber that would be crossed by particles independent of η in order to achieve a uniform response in radius. However, the folding angle must be kept between 60^o and 120^o because of the properties of the materials. Thus, it is impossible to cover the full pseudorapidity range with only one accordion structure. Therefore, each EMEC is made up of two coaxial wheels (i.e. an inner wheel and an outer wheel) with a 3 mm crack in between at $\eta = 2.5$, as illustrated

in figure 3.2 and 3.3 that keeps the combined thickness of LAr and absorber approximately constant. The outer wheel has 768 pairs of absorbers and electrodes, whereas the inner wheel has 256 pairs of absorbers and electrodes, each aligned with every third element of the outer wheel.

The absorbers are made of lead plates clad with 0.20 mm thick layers of stainless steel with 0.15 mm thick layers of glass-fiber prepreg[1] adhesive as glue in between. The lead thickness is 1.7 mm and 2.2 mm in the outer wheel and inner wheel, respectively.

The readout electrodes are constructed of three layers of copper separated by insulating Kapton[2] polyimide sheets, and are centered between the absorbers by honeycomb spacers[3]. Figure 3.4 illustrates this structure of the readout electrode. The two external

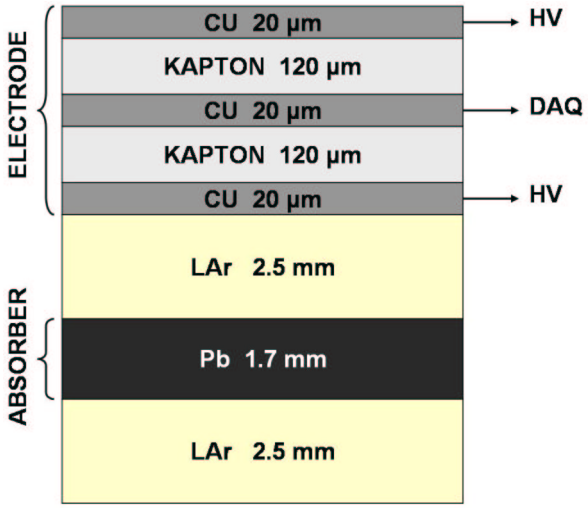

Figure 3.4: Schematic diagram of the readout electrode structure. HV stands for high voltage and DAQ stands for data acquisition system. Note that the material thicknesses are not to scale. The LAr-absorber-LAr-electrode pattern repeat in ϕ.

[1]BROCHIER SA, filiale CIBA-GEIGY, France.
[2]Kapton is a trade mark of Dupont Corporation.
[3]Fabrication details can be found in [19].

copper layers are connected to high voltage to produce the electric field needed to drift the ionization electrons in the LAr. The motion of ionization electrons induces currents that are collected on the inner copper layer by capacitive coupling. These readout electrodes are segmented into three longitudinal compartments (i.e. in depth along the beam axis) in the outer wheel and two longitudinal compartments in the inner wheel.

The readout towers are formed in η by etching copper strips on the three copper layers of the electrode. These copper strips are then segmented into three longitudinal compartments (i.e. in depth along the beam axis) in the outer wheel and two longitudinal compartments in the inner wheel. In the beam test, only the outer wheel module of the EMEC is used and the three longitudinal segments are to be referred as layer 1 (front, i.e. closest to the ATLAS interaction center), layer 2 (middle) and layer 3 (back) from here on. The longitudinal depths of these layers are approximately $4X_0$, $16X_0$ and $4X_0$ respectively.

By electrically connecting a number adjacent of electrodes in ϕ that are already segmented in η and in depth, a complete readout cell geometry is, then, defined, and connections to these cells are made directly at the front and rear faces of the calorimeter. For the outer wheel, the readout from layer 1 is routed to the front and the readout from layers 2 and 3 are routed to the back. This eliminates the cracks between channels providing excellent hermiticity and reduces the charge transfer time to the preamplifier by shortening readout lines and reducing their inductance.

There is a certain amount of dead material due to cables, cryostat walls, services, etc., equivalent to about 3-4X_0 in front of the EMEC. Therefore, a presampler (PS) was

placed in front of the EMEC in order to sample the showers started in the dead material. By appropriately weighting the energy observed in the PS, it is possible to partially compensate for energy lost before the EMEC. The PS consists of two 2 mm LAr layers formed by three electrodes parallel to the front face of the EMEC and is located 3625 mm from the ATLAS interaction center in front of the EMEC covering the $1.50 \leq |\eta| \leq 1.80$ region.

In ATLAS, particles produced at the interaction (collision) center will cover the full solid angle subtended by the detector. In order to improve the response of the detector, the readout cells are formed in such a way that they are fully (both in η and ϕ) pointing towards the ATLAS interaction center. In other words, if a minimum ionizing particle such as muon from the interaction center traverses the calorimeter, it will go through only one readout cell in each longitudinal segment, regardless of the direction it is coming. The three longitudinal compartments of the EMEC outer wheel have different η segmentations as is clearly visible in figure 3.5 which illustrates the active high voltage layer of an outer electrode. The geometrical layout of the readout cells in the PS and the layer 1, layer 2 and layer 3 of the EMEC outer wheel are presented in figures 3.6, 3.7, 3.8 and 3.9. The numbered cells shown are the ones instrumented (read-out) and used in the beam test. Geometrical dimensions of a cell in each layer are given in table 3.1. The η region, $1.5 \leq |\eta| \leq 1.8$,

Region	Layer	$\Delta\eta$ (rad)	$\Delta\phi$ (rad)	Δx (cm)	Δy (cm)	Δz (cm)
$1.5 \leq \|\eta\| \leq 1.8$	PS	0.025	0.1	16.8	4.2	0.5
	1	0.025/8	0.1	16.8	0.525	8.5
	2	0.025	0.025	4.2	4.2	34.0
	3	0.050	0.025	4.2	8.4	8.5

Table 3.1: Geometrical dimensions of a readout cell.

covered in the beam test corresponds to the region in θ from 0.44 to 0.33 in radians (25 to 19 in degrees).

In the beam test, the particles were incident perpendicular to the front face of the calorimeter so that the test setup (details are discussed in Chapter 4) was not aligned with the pointing geometry in η in contrast to the normal orientation in ATLAS. Therefore, EM showers systematically shift to different towers in η as a function of depth making the analysis extremely difficult. However, the towers are still correctly oriented in ϕ, so the position resolution of the EMEC is assessed only in the ϕ direction. The layer 2 of the EMEC is used for the purpose of the position reconstruction due to its fine segmentation in ϕ and the fact that the largest fraction of the deposited energy is contained in this layer as it is the thickest and is located where the shower density is maximized. The very fine η segmentation of layer 1 is also used in the event selection as shall be seen in Chapter 5.

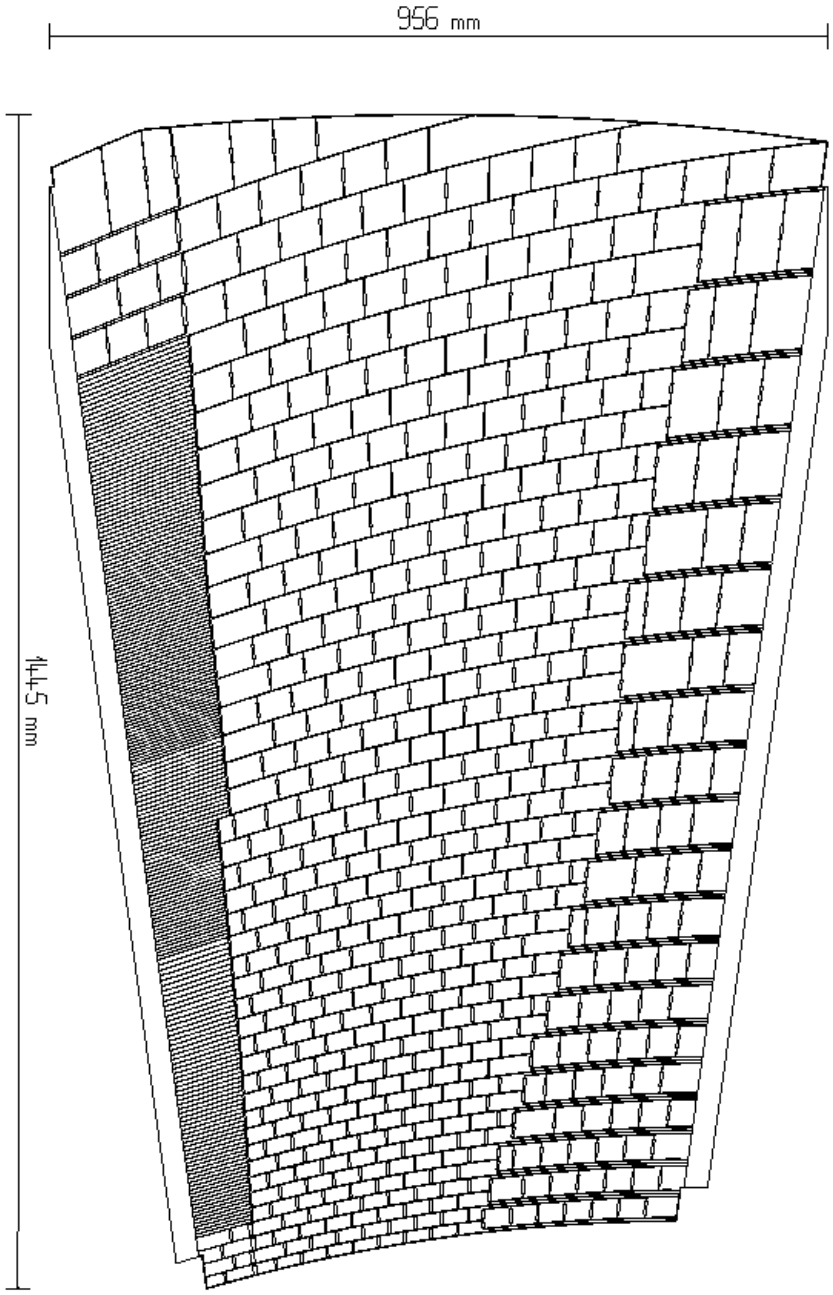

Figure 3.5: High voltage layer of an electrode of the EMEC outer wheel before folding into its accordion shape. The three longitudinal layers with different η segmentations are visible.

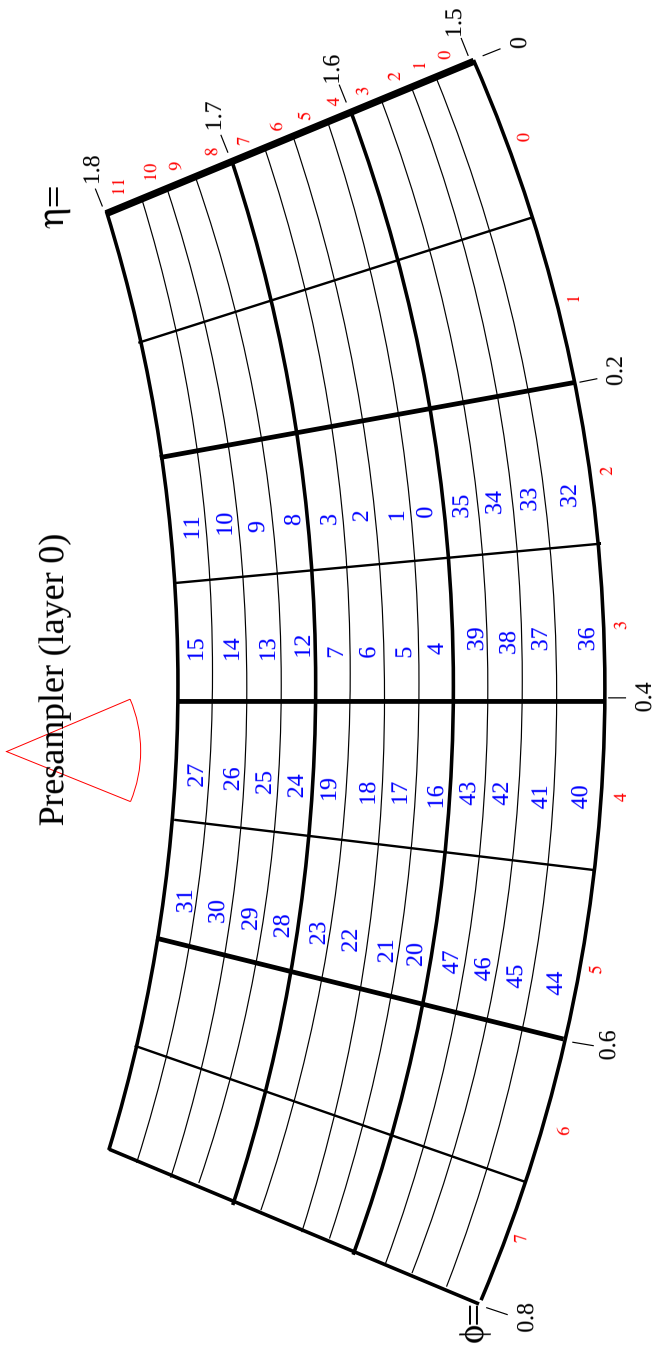

Figure 3.6: Layout of the instrumented readout channels of the PS. Shown are the front face of each channel with their corresponding cell number.

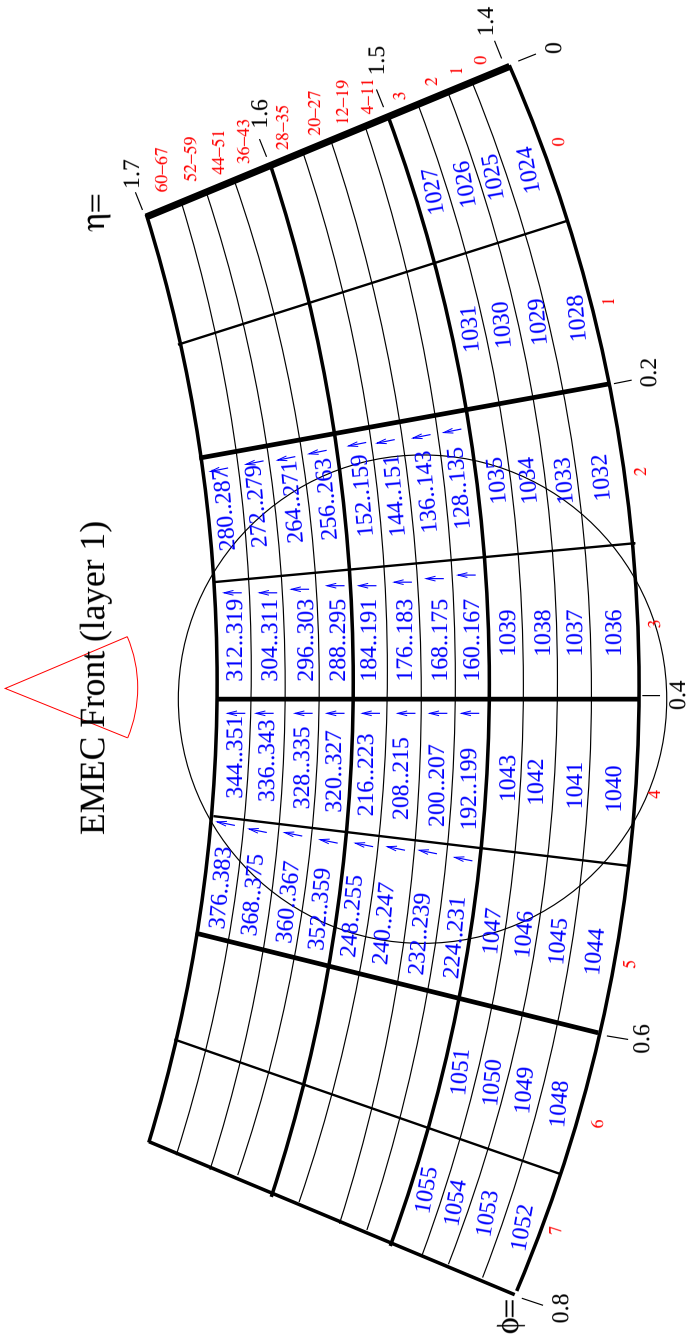

Figure 3.7: Layout of the instrumented readout channels of the EMEC Layer 1. Shown are the front face of each channel with their corresponding cell number. Note that there are actually 8 cells on each row above $\eta = 1.5$. The circle denotes the cryostat window.

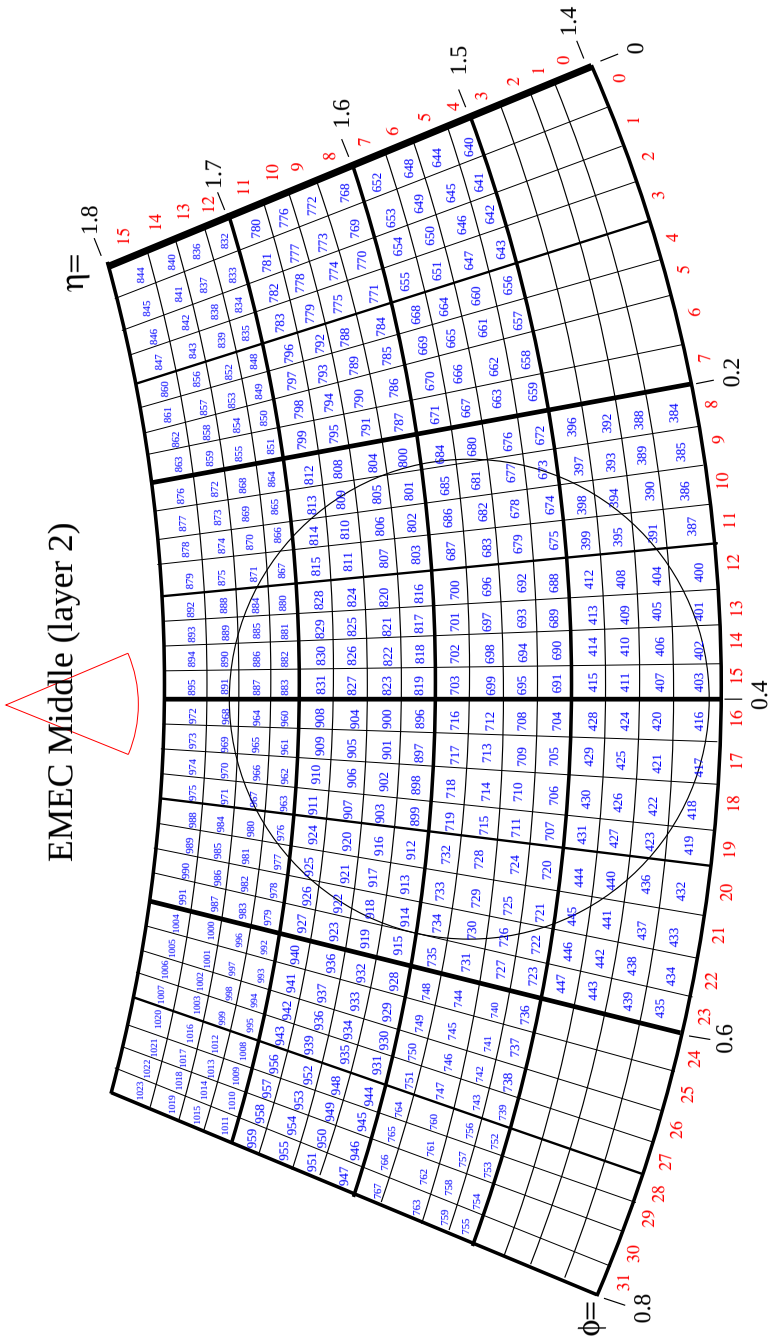

Figure 3.8: Layout of the instrumented readout channels of the EMEC Layer 2. Shown are the front face of each channel with their corresponding cell number. The circle denotes the cryostat window.

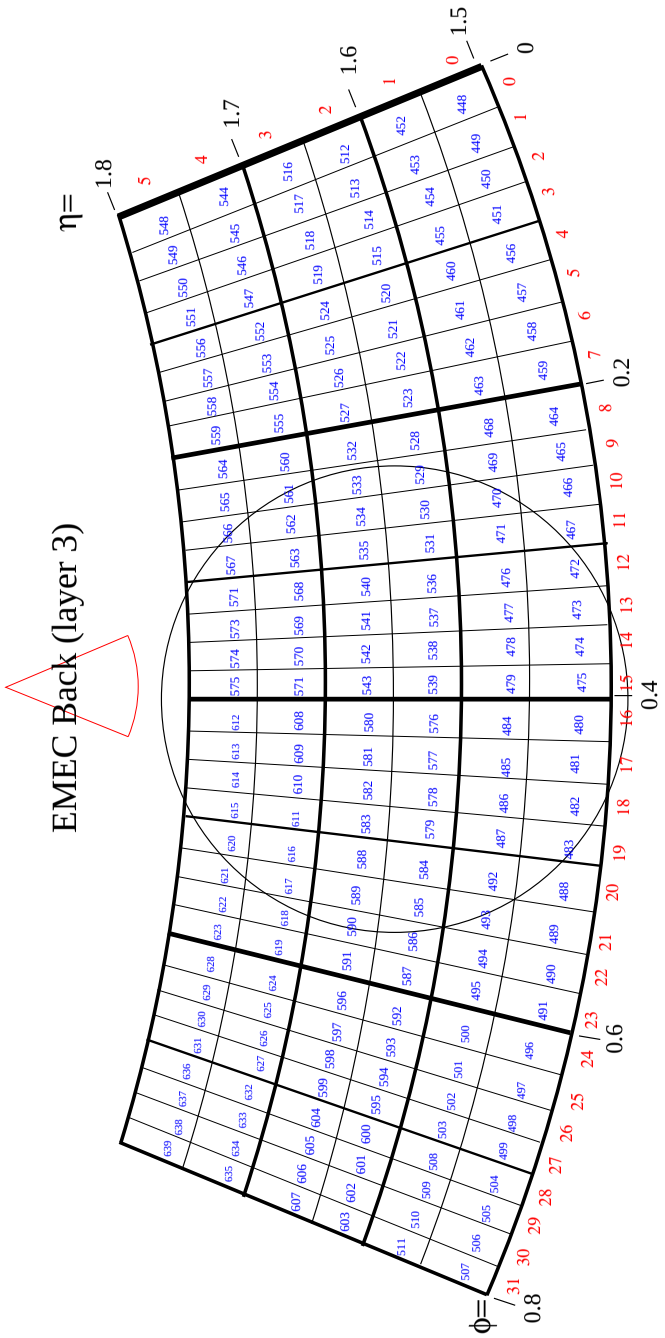

Figure 3.9: Layout of the instrumented readout channels of the EMEC Layer 3. Shown are the front face of each channel with their corresponding cell number. The circle denotes the cryostat window.

Chapter 4

Beam Test

In the summer of 2002, sections of EMEC and HEC modules, identical to those installed in the actual ATLAS detector, were exposed to beams of electrons, positrons, pions, and muons with energies in the range between 6 GeV $\leq E \leq$ 200 GeV in the H6 beam line in the North Area at the CERN SPS. The section of the ATLAS detector studied corresponds to the pseudorapidity interval $1.6 \leq |\eta| \leq 1.8$. For this work, data collected with electron beams directed towards several impact positions on the calorimeter face (see appendix A) with 10 energies ranging from 6 GeV to 148 GeV are analyzed to assess the position resolution of the EMEC.

The general experimental setup including the coordinate system unique to this beam test is described and a brief explanation of the signal reconstruction process is discussed in this chapter.

4.1 Experimental Setup

The combined beam test consisted of the outer section (large radius) of one EMEC module including the PS (1/8 of the full EMEC wheel), three HEC1 modules(3/32 of the full HEC1

wheel) and two half depth HEC2 modules installed in a cryostat which was filled with LAr up to a height of 2.20 m. The general setup of the experiment is illustrated in Figure 4.1.

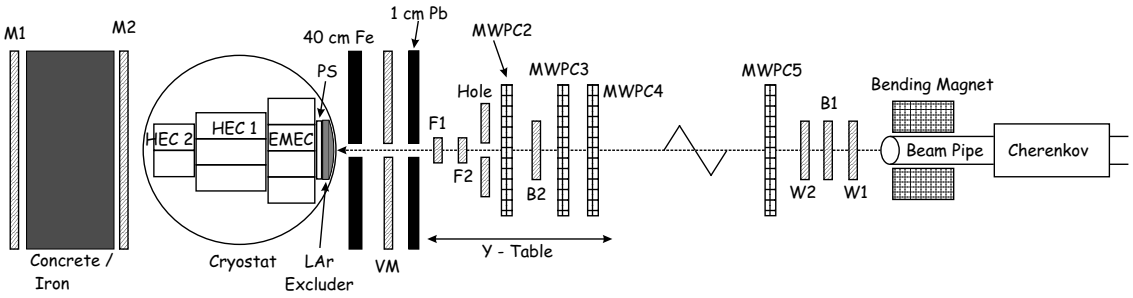

Figure 4.1: Schematic view of the layout of the EMEC and the HEC modules as well as the beam instrumentation used in the experimental setup of the beam test.

The cryostat is a stainless steel cylinder with an inner diameter of 2.50 m. There is a circular beam window with a reduced thickness (5.5 mm stainless steel) and a diameter of 60 cm. This results in a usable area of 60×50 cm^2 available for horizontal and vertical scans because the cryostat can be moved horizontally by ± 30 cm and a bending magnet allows for a vertical deflection of the beam by ± 25 cm at the front face of the cryostat. Due to the constraint imposed by the cryostat dimensions, the longitudinal depth of the HEC2 modules were limited to half of those in ATLAS and neither the cryostat nor the calorimeter modules were tilted (approximately 22 degrees) with respect to the beam line in order to produce the ATLAS-like pointing geometry in η. Instead, the impact angle of the beam particles was essentially perpendicular to the calorimeter module faces. Figure 4.2 shows the top view of the cryostat in which the PS, the EMEC module, the three HEC1 modules and the two HEC2 modules positioned from left to right respectively.

Event[1] selection is made using the Cherenkov counter [22] (up to 80 GeV only), the

[1] An event is the occurrence of a single beam particle interacting with the calorimeter materials in this

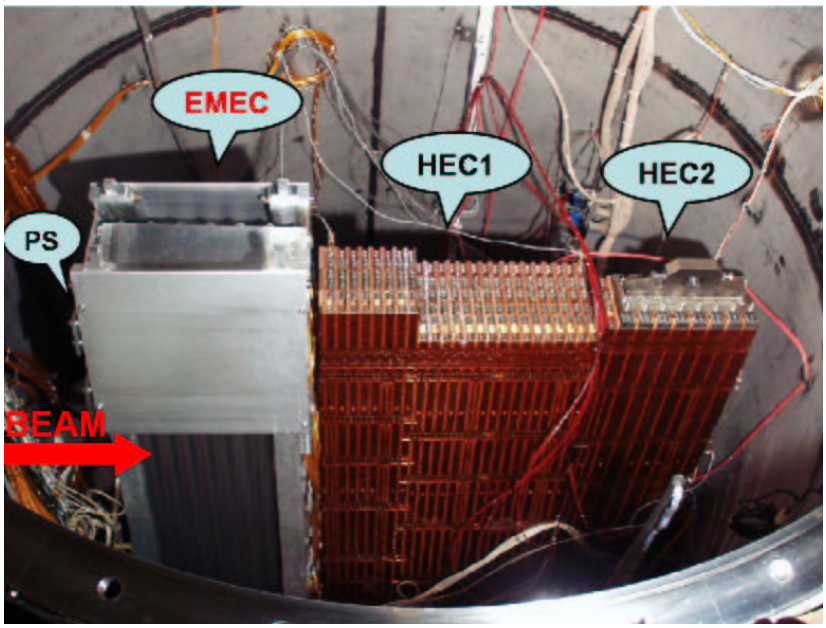

Figure 4.2: Top view of the beam test cryostat. The presampler, the EMEC module, the three HEC1 modules and the two HEC2 modules are positioned from left to right respectively.

scintillation counters B1, F1, F2 and the scintillation walls VM, M1, M2 located in front and behind the cryostat. Figure 4.1 shows the locations of these detectors. An event is pre-triggered by a coincident signal in the B1, F1 and F2 detectors. Geometrical dimensions of these detectors are given in table 4.1. The F1 and F2 counters are oriented perpendicular

Counter	Δx (cm)	Δy (cm)	Δz (cm)
B1	3.0	3.0	1.0
F1	2.0	2.0	2.0
F2	2.0	2.0	2.0

Table 4.1: Geometrical dimensions of the pre-trigger counters.

to each other and define the transverse size of the beam for triggered events. They are

beam test.

mounted on a table (y-table) which can be moved vertically to compensate when the beam is deflected up and down. The veto wall VM is composed of multiple scintillating counters with apertures in the center coinciding with the cryostat window that are used to reject the beam particles outside of the nominal beam diameter. These rejected particles are known as halo particles or beam halo. Events that are occurred too closely in time are also not recorded since this would result in an overlap of the signals (i.e. event pile-up) in the calorimeters. The pre-triggered events that are neither halo particles nor pile-up are recorded as physics events (also referred as the physics triggers). Muon identification is done by including the M1 and M2 detectors [23]. There were other triggers taken and recorded in the data files as well. However, only the physics triggers are used in this analysis.

The beam impact position and the angle of the particles are determined from four multiwire proportional chambers with 1 mm (MWPC2, MWPC3, MWPC4) and 2 mm (MWPC5) wire spacing in two planes (horizontal and vertical) per chamber. The size of each MWPC is 16.8 cm in x, 16.8 cm in y and 3.3 cm in z.

4.1.1 The beam test coordinate system

The beam test coordinate system is a right handed Cartesian coordinate system with y axis vertically up and z axis horizontal running parallel in opposite direction to the motion of the particles in the test beam. The origin corresponds to the center of the cryostat window. It is the basis for the coordinate system of the particle track reconstruction using the beam chambers (MWPCs).

4.2 Signal Reconstruction

Particles traversing the calorimeter ionize the LAr and the motion of the ionization electrons in an applied electric field produces a current (see section 2.4 and 3.3.2). The current is amplified and transferred onto a capacitor as charge. The ADC sees a voltage, $V = QC$, which is recorded as signal. The signal from each electronic channel is sampled (recorded) every 25 ns by an ADC. Typically, 7 samples are stored for the EMEC whereas usually 16 samples are recorded for the HEC due to electronic limitations. The timing of the samples is arranged so that the first sample recorded is before the signal starts.

The response of a given readout cell is computed in four steps. First, the base level of the ADC for zero input (referred to as the pedestal) is calculated by averaging the first sampling value of each event over an entire run[2]. The obtained pedestal is, then, subtracted from the channel signal for all samples. After the pedestal subtraction, the optimal filtering method [24] is applied in order to estimate the amplitude of the signal (i.e. the response of the channel to the incident particle). Finally, the measured amplitude is converted from voltage (in ADC counts) into current (in nA) using coefficients obtained from a separate electronic calibration.

The electronic readout chain of the calorimeters is calibrated by injecting a pulse with known equivalent ion current onto the readout electrodes. The signal is sampled by an ADC in exactly the same way as for real signals and then processed offline for the pedestal subtraction and optimal filtering as if it were a real signal. A small correction is needed

[2]A run is a number of sequential events (average 10000) from the same energy test beam at the same impact point recorded in a file. The number of events in a run is chosen so that the data is collected in a few tens of minutes.

because the pulse shape used for the calibration is an exponential whereas the real signal has a triangular shape. The correction depends on the frequency response of the electronic readout chains and is calculated using an Inverse Laplace Transform method for the HEC and a Fast Fourier Transform method for the EMEC. Details of these techniques can be found in [25]. The end result is a parametrized curve relating ion current to ADC counts.

The 25 ns sampling of the ionization signal is done by an independent 40 MHz ADC clock in the beam test. However, the time of particle arrival at the calorimeter (i.e. the time of the pre-trigger) is asynchronous with respect to this sampling clock unlike in ATLAS[3]. Thus, the relative time difference between the pre-trigger and the sampling clock needs to be calculated to synchronize the time and therefore to maximize the precision of the optimal filtering method. The TDC that was supposed to provide the relative time difference did not work very well in the beam test, so a cubic interpolation is applied around the signal maximum in order to calculate the time of the signal maximum for each cell for a given event and these cell times are combined to get the time (to be referred as the global cubic time) of the event and determine the relative time difference. The disadvantage of using the global cubic timing is that it requires the signal of a given event be large enough for the cubic fit to work. Hence, the global cubic timing is not applicable to muons.

[3]In ATLAS, the trigger will be synchronized with the bunch crossings of every 25 ns provided by a 40 MHz RF system.

Chapter 5

Data Selection and Position Reconstruction

Calorimetry is associated with the precision measurement of the energy of particles. However, calorimeters can also provide excellent position information and hence particle direction if the origin of the particle is known. The physics of the LHC requires good energy resolution, position resolution and particle identification. Therefore, the EMEC, with its high granuality (as fine as $\Delta\eta = 0.025/8$ and $\Delta\phi = 0.025$), is also designed to obtain the position of particles which induce EM showers, especially photons that leave no ionization tracks and hence make it impossible to use the conventional ionization tracking chambers for this purpose. This chapter explains how the data was selected and the position of electrons and positrons in layer 2 of the EMEC was calculated.

The position information of an EM shower, hence the incident particle, in a given EMEC longitudinal segment can be obtained by finding the energy weighted barycentre of a cluster[1] in that segment. As was mentioned previously in section 3.3.2 and 4.1, the impact angle of particles was perpendicular with respect to the front face of the EMEC in

[1] A cluster is a group of readout cells that are selected that contain the energy of the EM shower.

the experimental setup so that the geometry in η, was non-pointing (unlike the real ATLAS situation) and, therefore, yields a geometrically biased (shifted) reconstructed position in η, corresponding to y in the beam test coordinate system. Nevertheless, the beam test setup provided a geometry in ϕ which is identical to that of ATLAS. Thus, only the position in ϕ, corresponding to x, is studied in this work. The calorimeter reconstructed position in ϕ can be formulated as

$$\phi_{\text{cal}} = \frac{\sum_i \phi_i E_i^n}{\sum_i E_i^n} \tag{5.1}$$

where ϕ_i and E_i are the barycentre position and the deposited energy of i^{th} channel in the cluster of a given segment, respectively. The power n of the energy is chosen to be unity in this analysis because it gives the best resolution (see figure 6.9 in section 6.2). This is the expected result when the radial extent of the shower is bigger than the readout cells. The theoretical calculation of the radial shower size is presented in appendix B.

In order to determine the position resolution of the EMEC to electrons, the reconstructed position calculated using the calorimeter must be compared, for many events, to an independent measurement of the position which is performed using the MWPCs. Each of the four MWPCs provide an x and y coordinate for every beam particle. A least squares fit is performed[2], independently for the x-z and the y-z planes in the beam test coordinate system, using the four measured points to calculate the parameters (intercept and slope) that define the particle trajectory which can then be extrapolated to any given depth in the calorimeter. The MWPC reconstructed x-position in a given depth z in the beam test

[2]The fit parameters were calculated at CERN using a computer program developed by the beam test collaboration (see section 5.1). These values are used unchanged in this thesis.

coordinates is, thus, expressed as

$$x_{\mathrm{mwpc}} = x_0 + x_1 z \tag{5.2}$$

where x_0 is the intercept and x_1 is the slope calculated by the least squares fit. A similar expression for y-position can be obtained by replacing x with y in the same equation 5.2. The uncertainty, σ_{mwpc}, of the position at the middle depth of the EMEC reconstructed by the MWPCs is 312 μm (0.18 mrad in the ATLAS coordinates), calculated in appendix C.

The analysis carried out to assess the performance of the EMEC in terms of its position resolution to electrons can be divided into three main stages which involve three basic tasks: run selection, event selection and clustering. For convenience, the beam test coordinate system is the preferred reference frame until the very final stage. In the subsequent sections of this chapter, the analysis tools used in this project and the three stages mentioned above are discussed in detail.

5.1 Analysis Tools

There are two main analysis tools used in this project. The signal reconstruction of each cell for every event and the particle trajectory reconstruction is performed in the ATLAS ATHENA [26] computer program. ATHENA is a C++ [27] based object oriented framework designed and being developed by the ATLAS Collaboration to integrate all data processing steps (i.e. calibration, reconstruction, simulation, etc.) for consistent treatment of the data. The output of ATHENA is the reconstructed data stored in a ROOT [28] file for each run. ROOT is a general purpose data handling program developed at CERN based on C++. The information stored in an ATHENA output ROOT file can be summarized in

three main categories: standard information for all runs, global information specific for that particular run and event information specific to each event in the run (see table 5.1). The analysis discussed in the following sections is performed on these ROOT files using algorithms written by the author of this thesis within TBRootAna [29], a ROOT derived software package developed by the University of Victoria ATLAS Group for the analysis of ATHENA output ROOT files.

Standard Information	Global Information
total number of cells	run number
energy unit	beam energy
pedestal rms per cell	cryostat x-position
indexed cell positions	table y-position
miscellaneous	particle type
Event Information	
event number	
trigger response	
energy per cell	
global cubic time and rms	
TDC time	
MWPC fit parameters with error matrix elements	

Table 5.1: The information stored in an ATHENA output ROOT file.

5.2 Stage I – Run Selection

A temporary setup of a complex and sophisticated system, like the beam test, designed for another configuration (the real ATLAS experiment) causes challenges. Difficulties with the hardware and software during data taking and signal reconstruction resulted in problems with the data. In other words, there are datasets[3] which contain none or little physical data (i.e. a nonzero signal) due to, for example, a failure of the equipment in the setup.

[3]There is a single unique dataset for each run.

Therefore, it is necessary to have an initial look at the entire reconstructed data (i.e. all the runs) to find problem runs and eliminate them.

In order to make such a selection, each electron run is processed with a computer program and a run statistics database (i.e. a ROOT file) is formed. The initial processing of the electron runs[4] involved introducing the following four basic selection criteria (known as a *cut*) on an event by event basis;

(i) Non-physics triggers are ignored. Data with different triggers were collected simultaneously and flagged in the data file. However, only the physics events are included in the analysis. The physics trigger was described in section 4.1.

(ii) Events with failed global cubic time reconstruction are skipped. They are recognized because each has a global cubic time sigma of zero as a result of this problem.

(iii) Events with failed particle trajectory reconstruction using MWPCs (i.e. the least squares fit fails) are skipped. The fit parameters are set to the values (i.e. 999) that they are initialized with, when the least squares fit fails.

(iv) Cells with failed signal reconstruction are not used in calculating the total deposited energy in the calorimeter. When the signal reconstruction fails for a particular cell, it is set to a value of 3.402×10^{38} (maximum positive floating point value possible on a 32 bit machine).

The run statistics database is filled with the global information already available (see table 5.1) and the information given in table 5.2 that is derived in the initial processing of

[4]The beam transport parameters were set to produce nearly pure beams of electrons.

the data for each run. The total number of events are counted before the application of the

Basic Cut Statistics
total number of events
total number of physics events
total number of events with failed global time reconstruction
total number of events with failed particle trajectory reconstruction
Statistical Quantities Calculated
mean and rms of the MWPC reconstructed x_0-position
mean and rms of the MWPC reconstructed y_0-position
mean calorimeter reconstructed x-position at middle depth of layer 2
mean calorimeter reconstructed y-position at middle depth of layer 1
mean MWPC reconstructed x-position at middle depth of layer 2
mean MWPC reconstructed y-position at middle depth of in layer 1
mean and rms of the global cubic time
mean deposited energy in PS
mean deposited energy in layer 1
mean deposited energy in layer 2
mean deposited energy in layer 3
mean total deposited energy in EMEC
mean total deposited energy in HEC

Table 5.2: The information stored in the run statistics database for each run along with the global information already available.

basic cuts above. Then, the first cut (i) is applied and the total number of physics events that survived the cut are counted. The second cut (ii) is applied on the physics events and the total number of events with failed global cubic time reconstruction that are skipped are counted. The third cut (iii) is applied on the events that survived the first two cuts and the total number of events ignored with failed particle trajectory reconstruction are counted. Consequently, the statistical quantities (see table 5.2) are calculated from the events that survived the first three basic cuts and using all of the instrumented cells that passed the last cut (iv). At the same time, the distribution of each statistical quantity is entered into a histogram and stored in another ROOT file. The histograms were examined in order to

verify data quality. They were also useful for debugging during the whole analysis chain but were not used to make any cuts. An example of such histogram is given in figure 5.1.

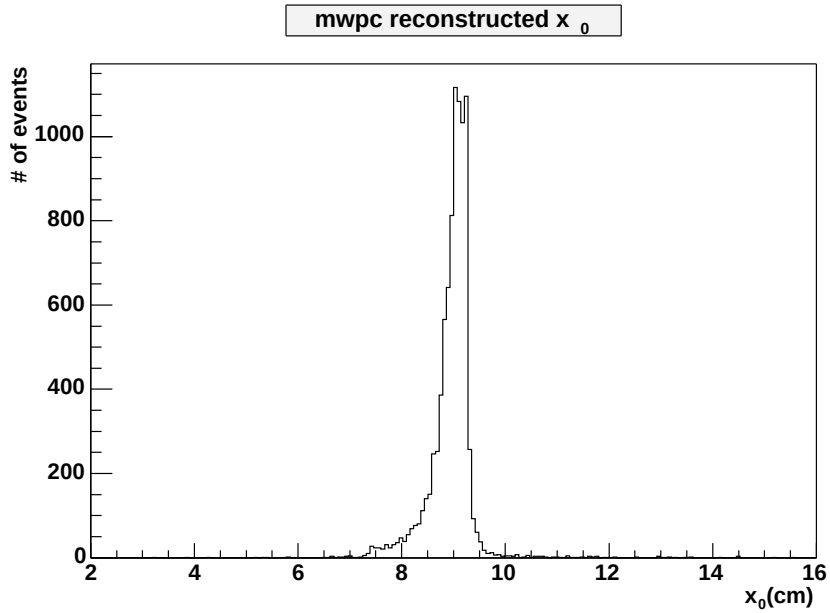

Figure 5.1: The MPWC reconstructed x_0-position of 119 GeV electrons at impact point J.

Finally, using the information from the database, runs are eliminated where more than 95% of the total physics events have either or both failed global cubic time and failed particle trajectory reconstructions. These runs are eliminated because the lack of physical data would yield statistical errors that are too large to give a reliable position resolution determination. The runs removed from the analysis up to this point correspond to no more than 2% of the total number of runs (total runs before/after = 188/185).

5.3 Stage II – Event Selection

After selecting the datasets to be analyzed, the next important task is to select events that are due to electrons impinging on the EMEC while still ignoring the poorly reconstructed

events (bad events) and the cells (bad cells). The EMEC is optimized for EM showers as previously discussed in chapter 2. This thesis will only consider the position resolution for electrons and positrons.

Electrons deposit their energy through EM processes and are fully contained in the EMEC. Charged pions lose energy mostly through hadronic processes and are, therefore, usually not contained by the EMEC alone but rather by both the HEC and the EMEC. Hence, energy will be observed in the HEC and there will be less energy in the EMEC than one would see for an electron. Muons, on the other hand, deposit only a very small amount of their energy in both calorimeters through ionization. So, in order to select electrons, it is necessary to estimate the total energy deposited in the EMEC and the HEC and to compare the two. Total energy is calculated for this purpose by summing the energy of all the good cells in the EMEC and the HEC respectively. In figure 5.2, the energy response of the EMEC (upper plot) and the 2-dimensional view of the total energy response in both calorimeters (lower plot) to a 119 GeV electron beam can be seen. Three populations of particles (e, π, μ) in the beam can clearly be observed on both histograms and electron events are easily identified in a narrow peak at high energy in the EMEC in the upper plot. Since, there are no pions or muons to the right of that narrow peak, the distance (in terms of nA) from the highest peak position to the maximum deposited energy seen in the EMEC energy response histogram is calculated and, then, is symmetrically projected to the left of the peak to determine the full width of the electron energy distribution. All of the events outside this range are ignored. The result of this selection is given in figure 5.3. It is important to note that there is still some ($\approx 0.1\%$) pion contamination under the electron

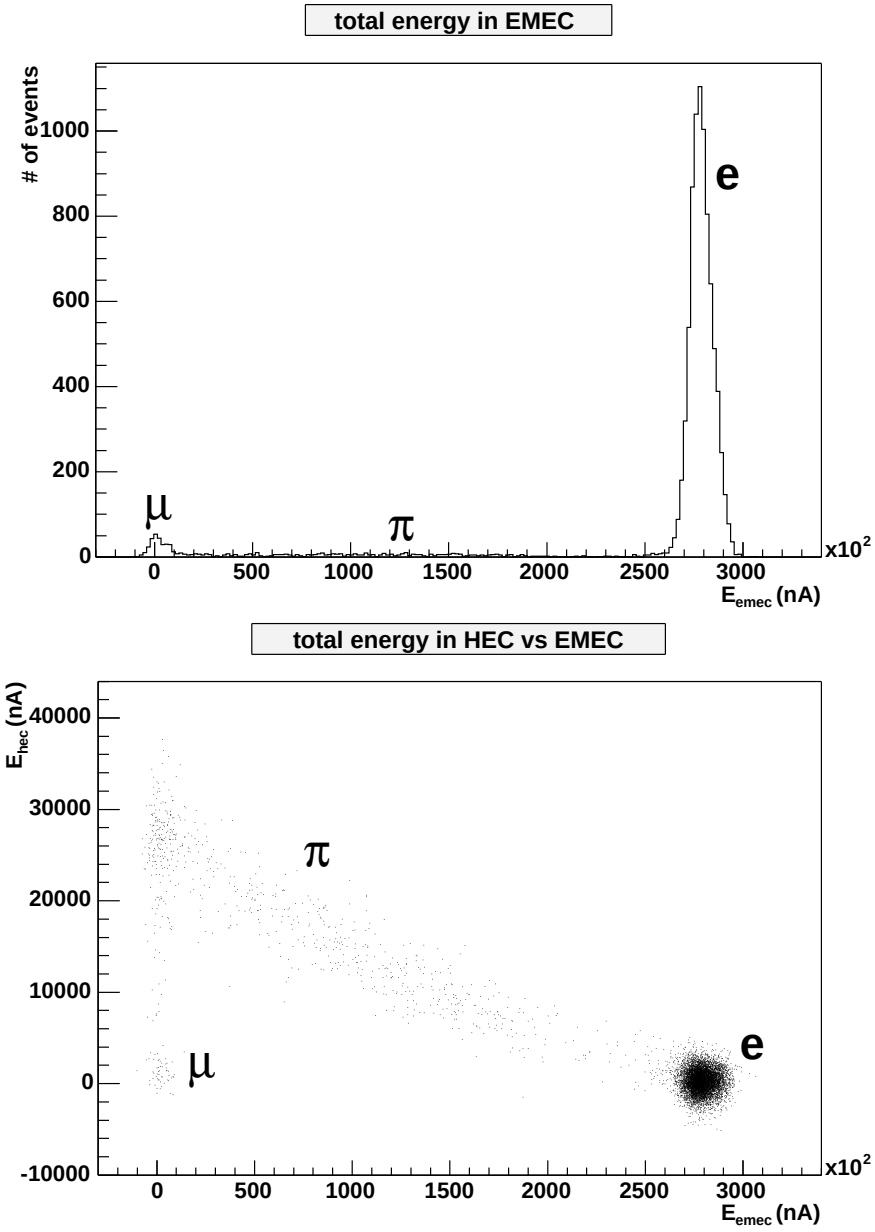

Figure 5.2: The energy response of the EMEC (upper plot) and the 2-dimensional scatter histogram (lower plot) of the total energy response of the HEC versus the total energy of the EMEC to a 119 GeV electron beam at impact point J.

peak. The level of this contamination is estimated by looking at a 119 GeV pion beam distribution and extrapolating the pion distribution under that electron peak. However,

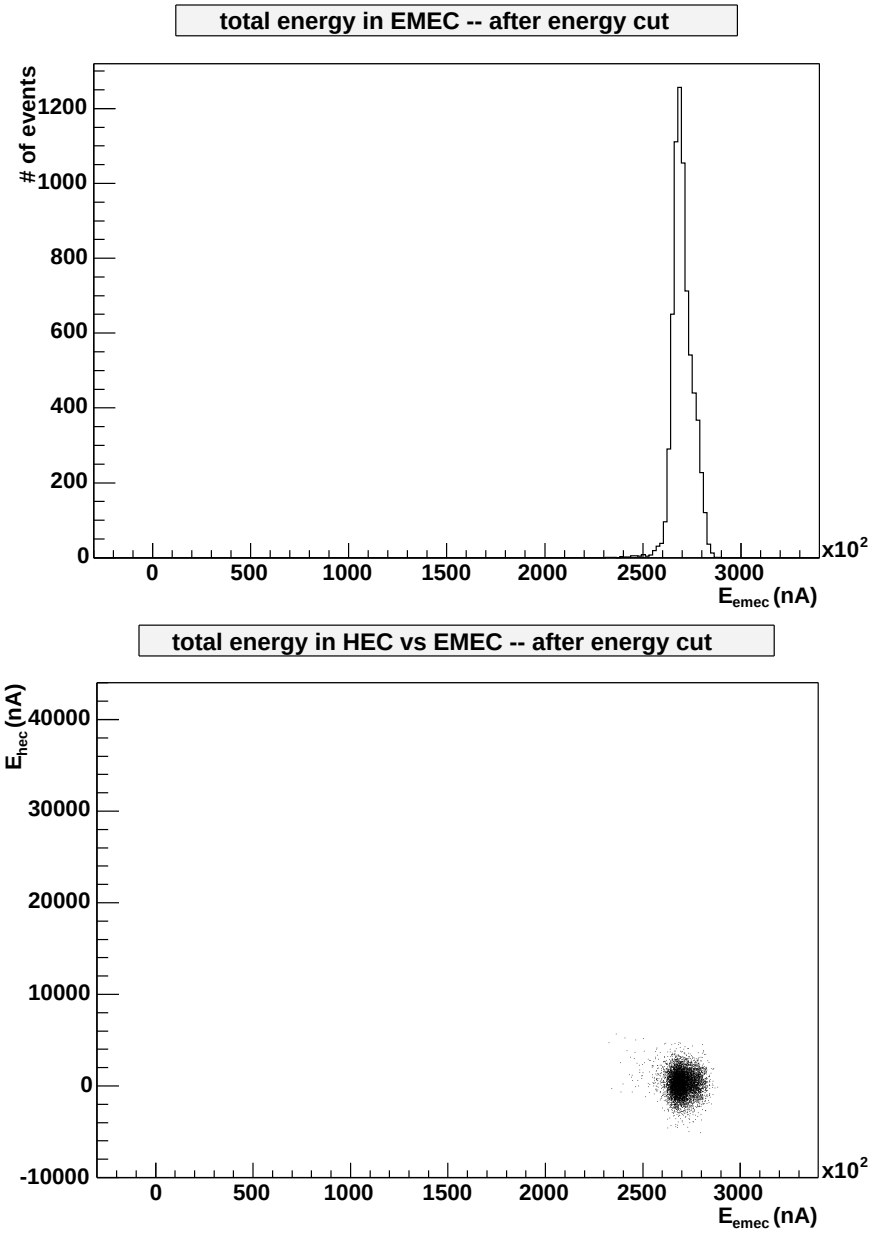

Figure 5.3: The energy response of the EMEC (upper plot) and the 2-dimensional view of the total energy response in both calorimeters (lower plot) to 119 GeV selected electron events at impact point J. A small amount of residual contamination is seen but is expected to have a negligible effect on the final result.

this contamination is very small and these are the charged pions that must have deposited their energy mainly via EM processes. Thus, they would have no degrading effect on the position resolution being essentially electron like.

At this point in the analysis, the first comparison between the reconstructed position using the MWPCs and the layer 2 of the EMEC at middle depth of the layer 2 in the beam test coordinate system is made. The EMEC middle segment is used due to its fine granularity and largest thickness (see section 3.3.2). It is also where the shower maximum is. Therefore, it contains the largest fraction of the total deposited energy in the EMEC and gives the best ϕ position information when using the energy weighted barycentre to determine the position of the shower. Figure 5.4 shows a good example of the position measured by the calorimeter compared to a measurement by the MWPCs. The upper plot shows the strong correlation between the calorimeter reconstructed position in x (corresponding to ϕ in ATLAS) and the MWPC reconstructed position. The lower plot shows the gaussian-like distribution of the difference between the two independent methods of position reconstruction. About 70% of the runs analyzed are of this quality. Unfortunately, this is not the case for the runs in the energy range from 40 GeV to 80 GeV as can be seen in the example in figure 5.5. Although, the high sharp peak under which the expected correlated events are distributed in the center of the lower histogram can clearly be seen, the rest of the uncorrelated events are of concern. No physical explanation was found for such a behavior. Most likely, there was an error or failure in the trigger electronics. It is possible to exclude most of the unwanted events from the rest of the analysis by making a cut in the $y-z$ plane on the reconstructed position information given by MWPCs, since the

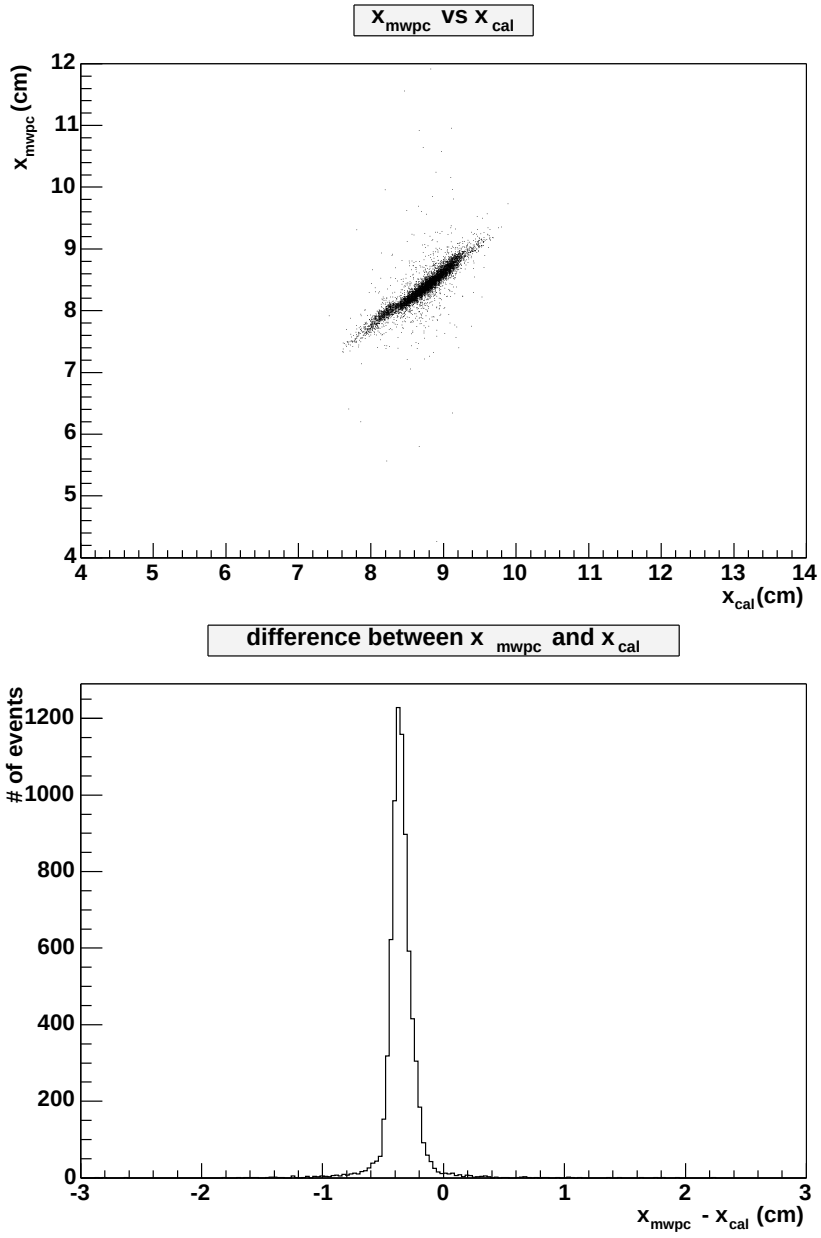

Figure 5.4: A 2-dimensional comparison (upper plot) of the x-position of a 148 GeV electron beam at impact point J given by the MWPCs and the layer 2 of the EMEC as well as the difference (lower plot) of these two independent measurements at the middle depth of the layer 2.

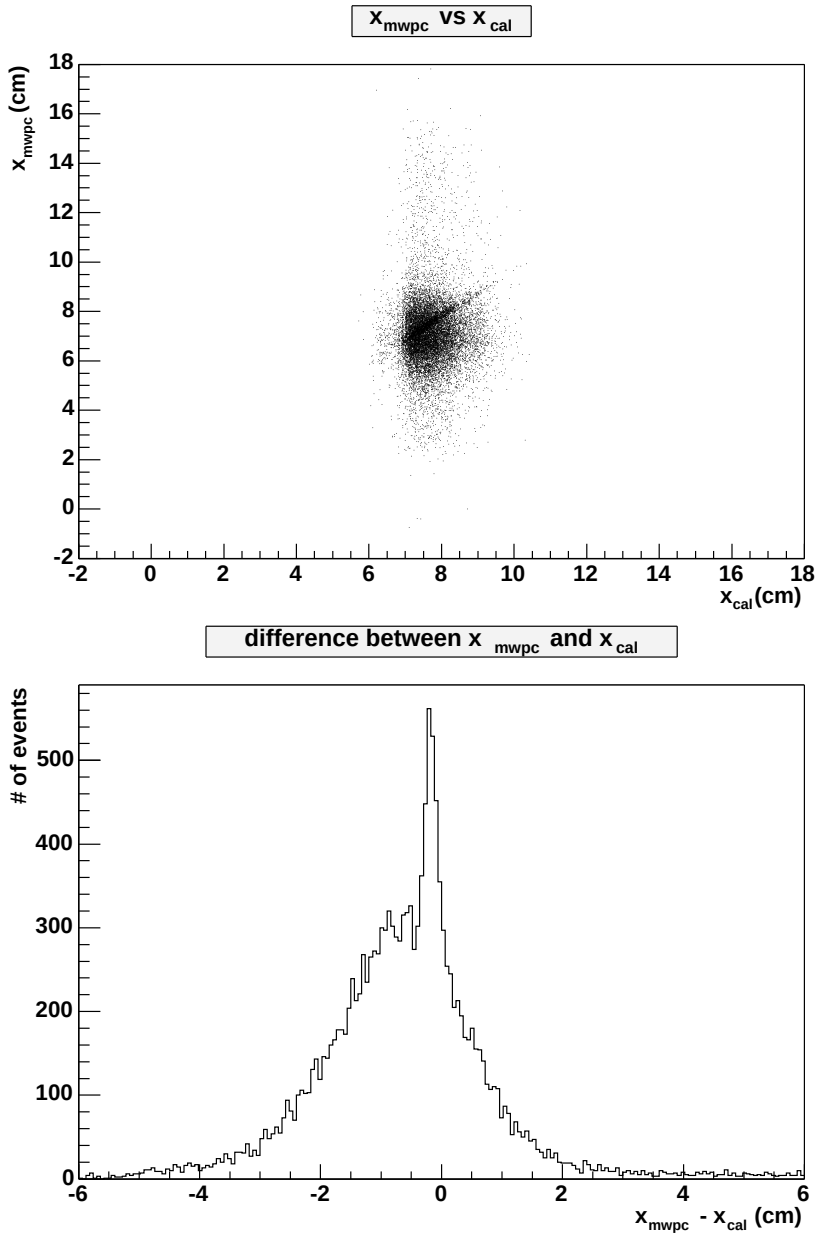

Figure 5.5: A 2-dimensional comparison (upper plot) of the x-position of a 60 GeV electron beam at impact point J given by the MWPCs and the layer 2 of the EMEC as well as the difference (lower plot) of these two independent measurements at the middle depth of the layer 2. A hint of events (lower plot) with a correlation between the calculated x-position using MWPCs and layer 2 can be seen.

particle trajectories that are found via least squares fits on the $y-z$ and the $x-z$ planes are independent. For this purpose, the y-position of the beam is reconstructed from the layer 1 of the EMEC because of the very fine granuality of layer 1 of the EMEC in y (corresponding to η in ATLAS). In figure 5.6, a highly correlated area at the top end of the dark blob of events can be seen despite the large background. By moving a 2.5 cm window in y

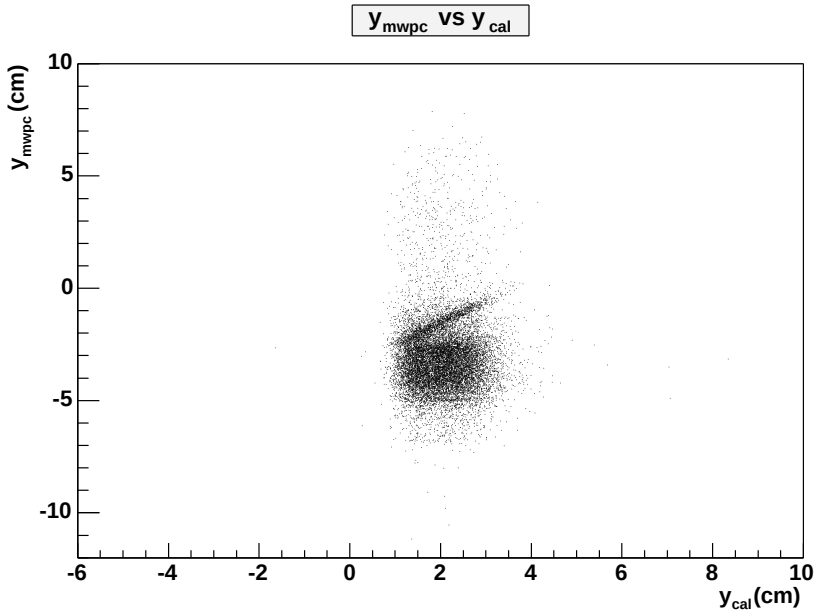

Figure 5.6: A 2-dimensional comparison of the y-position of a 60 GeV electron beam at impact point J given by the MWPCs and the layer 1 of the EMEC at the middle depth of the layer 1.

down the vertical axis in 0.25 cm steps and calculating the correlation within the window at each step, the events in the window with the maximum correlation are selected for the final stage of the analysis. The same histograms as shown in figure 5.5 is recalculated after the correlation cut and presented in figure 5.7. A clear improvement is seen. Consequently, all of the data files (i.e. ATHENA output ROOT files. See section 5.1) are reproduced with

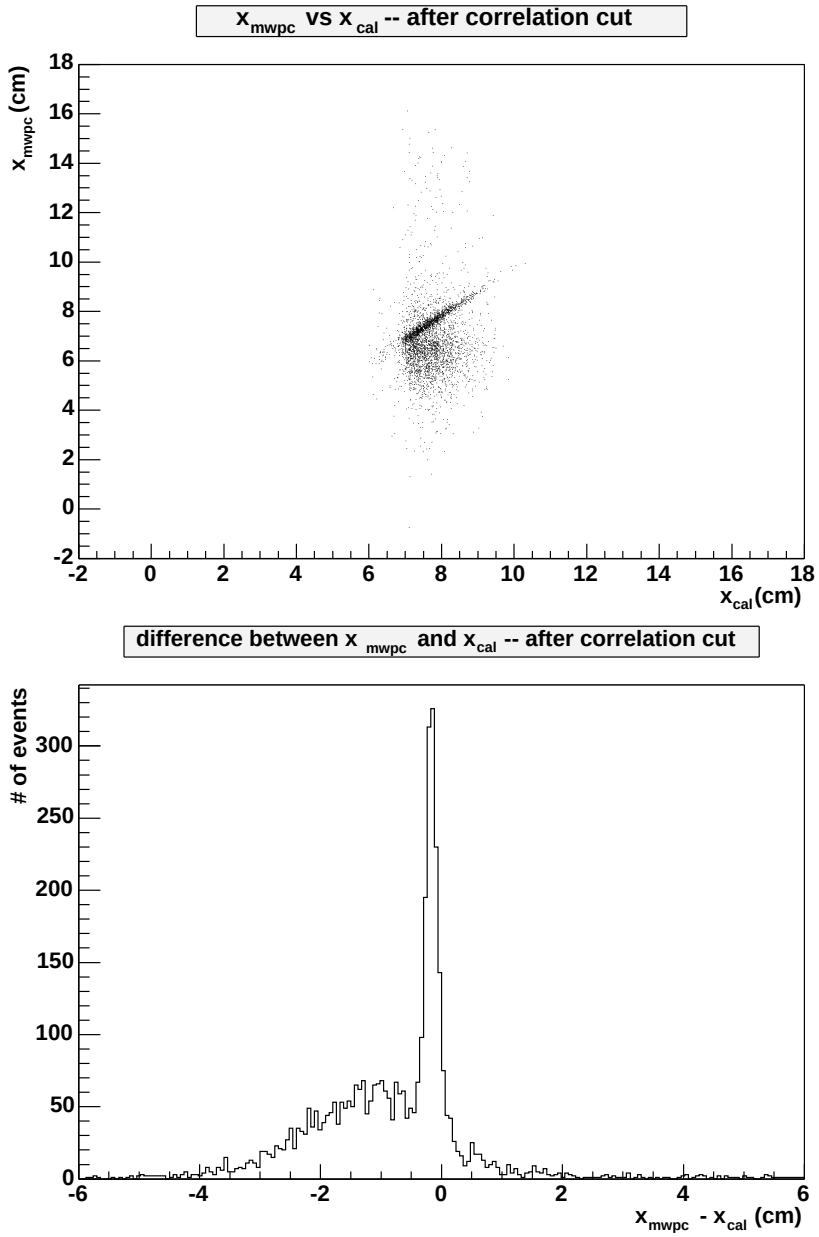

Figure 5.7: A 2-dimensional comparison (upper plot) of the x-position of a 60 GeV electron beam at impact point J given by the MWPCs and the layer 2 of the EMEC as well as the difference (lower plot) of these two independent measurements at the middle of the layer 2 after the correlation cut. Same data of figure 5.5 and 5.6. A clear improvement is seen compared to figure 5.5.

only the events that survive all the cuts been made thus far including the correlation cut for each run. These new ROOT files are used for the rest of the analysis.

At 100 GeV, there are no runs with a reasonable number of events to further the analysis after the correlation cut, consequently all of the runs at this energy level are excluded from this work (total runs before/after = 185/176). There is a large number of runs at 119 GeV. Three of these runs give at least 10% lower energy in EMEC compared to the others. There was no explanation, so these three runs are eliminated as well (total runs before/after = 176/173).

5.4 Stage III – Clustering

The lateral electromagnetic shower size of approximately 15.4 cm (for 95% containment), calculated in appendix B, is much smaller than the full EMEC module but bigger than one readout cell. Hence, several cells must be summed to collect all of the signal. Since each readout cell has a random signal associated with it due to electronic noise, adding all the cells in the calorimeter, when calculating the response, increases the total electronic noise contribution. This is particularly true because many cells have no real energy deposited in them. Therefore, in the final stage of this study, a clustering algorithm is applied to select cells with real energy in order to reduce the electronic noise contribution to the EMEC energy response and hence to improve the accuracy of the calorimeter reconstructed position. In general, clustering algorithms rely on selecting only geometrically contiguous cells that are centered on the axis of the shower and have some energy deposited above an average noise level.

In this thesis, the clustering algorithm makes use of the standard deviation, σ_{noise}, of the electronic noise. A noise algorithm was developed [30] to calculate the σ_{noise} of each channel for a given run. The readout cells of a given run must first be categorized by the noise algorithm as empty cells (with no energy) or cells with energy deposition (hit cells). The reconstructed signal distribution of an empty cell peaks at or very near zero (see figure 5.8) representing the noise of the cell. In order to distinguish hit cells, the signal

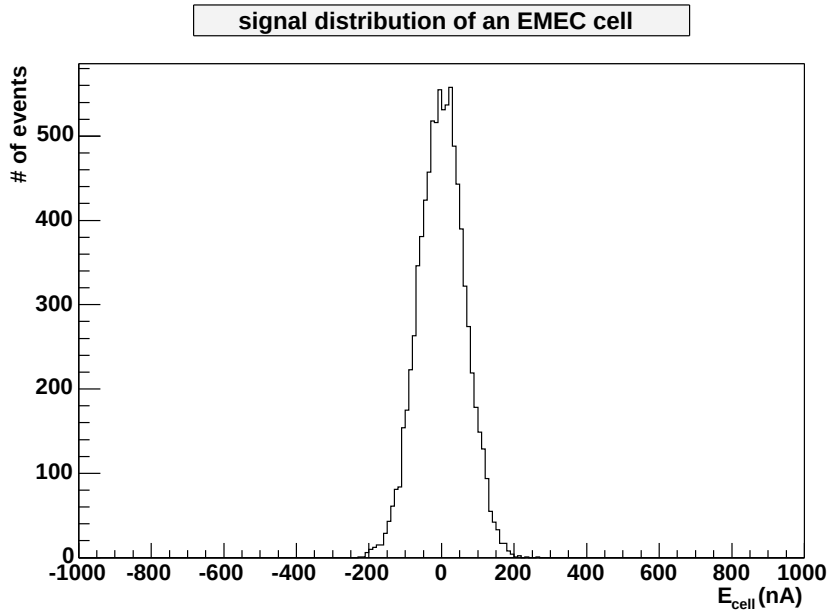

Figure 5.8: The reconstructed signal distribution of a cell with no energy.

distribution of each cell is entered into a histogram, and a gaussian fit in the range from -1000 nA to 1000 nA (noise region) is applied to each histogram. The following parameters are defined;

$$\mu_{\text{dif}} = |\mu_{\text{h}} - \mu_{\text{g}}| \ , \ \mu_{\text{cut}} = 10 \text{ nA} \ , \ \sigma_{\text{cut}} = 3 \times \sigma_{\text{g}}$$

where μ_{h} is the mean of the histogram, μ_{g} and σ_{g} are the mean and the error of the gaussian

fit. If $\mu_{\rm dif} > \sigma_{\rm cut}$ and $|\mu_{\rm h}| > \mu_{\rm cut}$ for a given cell, then it is identified as hit cell. Once the categorization of cells is complete, each empty cell is assigned the width of its gaussian fit as $\sigma_{\rm noise}$.

For the calculation of the hit cell $\sigma_{\rm noise}$, the noise algorithm makes use of the pedestals. Recall section 4.2, the first sample of each pulse is used to estimate the baseline value for a cell signal for each event. The mean value of the baseline is the pedestal and the root mean square deviation, $rms_{\rm ped}$, is an estimate of the noise. The high voltage supplied to the EMEC electrodes is uniform. However, the cell volume and hence the capacitance is different at each η slice (see figure 3.8 for example) due to the cylindrical segmentation of the EMEC. Therefore, one can expect the level of electronic noise to depend on η. In order to estimate the $\sigma_{\rm noise}$ for hit cells in each η slice, the following parameter is defined;

$$r = \frac{\sigma_{\rm noise}}{rms_{\rm ped}}$$

where $rms_{\rm ped}$ is the pedestal rms of a cell. Finally, the $\sigma_{\rm noise}$ of a hit cell in a particular η slice is found by the product of the $rms_{\rm ped}$ of the hit cell and the average of the ratio r of all empty cells in that η slice. The reason for averaging the ratio r instead of just $\sigma_{\rm noise}$ is to reduce the effect of potentially noisy cells since the pedestal rms of such cells would be proportionally high as well.

The clustering algorithm consists of four steps to determine the group of hit cells to be used to reconstruct the position for a given event in a run;

(i) Determine the cell with the maximum energy deposited for each layer for each event.

(ii) Look at the entire run and select the cell (to be referred as the seed cell) which has

the maximum energy deposited the most number of times for each layer.

(iii) Form a rectangular area (11×3 in Layer 1, 7×7 in Layer 2, 5×9 in Layer 3)[5] where the seed cell is the center. The size of the rectangular area in each layer is determined by the expected lateral size of the shower (see appendix B).

(iv) Select only the cells in the rectangular area with deposited energy absolute value more than $2\sigma_{\text{noise}}$.

The calorimeter reconstructed position of an event is calculated using equation 5.1 where the sum is over only the cells selected by this so called fixed clustering method described above.

Finally, the MWPC reconstructed x-position in the beam test coordinates found by equation 5.2 is transformed into ϕ in the ATLAS coordinate system as well to allow comparison of the two independently reconstructed positions. The transformation of a point between the two (beam test and the ATLAS) coordinate systems is achieved using a passive y-convention Euler rotation [31] and a translation;

$$X = \begin{pmatrix} x \\ y \\ z \end{pmatrix} = R_{z''}(\psi_\varepsilon) R_{y'}(\theta_\varepsilon) R_z(\phi_\varepsilon) X_{\text{L}} + X_0 \tag{5.3}$$

where $x_0 = 0$, $y_0 = 171.8$ cm, $z_0 = 298.3$ cm, $\phi_\varepsilon = \frac{5\pi}{8}$, $\theta_\varepsilon = \pi$, $\psi_\varepsilon = 0$, and X_{L} is the vector representation of the point in the ATLAS local Cartesian coordinate system that is defined for the EMEC module as a right handed system attached to the detector with x_L axis along the rightmost edge of the module, z_{L} axis in the direction of the test beam particles. The X_{L} can be represented in the cylindrical form using the following relations;

[5]The unit length is the size of a cell in each segment in η and ϕ

$$x_{\mathrm{L}} = \rho \cos \phi$$
$$y_{\mathrm{L}} = \rho \sin \phi$$
$$z_{\mathrm{L}} = \rho \sinh \eta$$

where ρ is the radius at which the point is on the EMEC wheel centered on the ATLAS detector beam axis. The $R_\alpha(\beta)$ represent a 3×3 rotation matrix about axis α by angle β. At $\eta = 1.6$, the size of a cell in layer 2 of EMEC is 4.26 cm in x and 0.0245 rad in ϕ.

Chapter 6

Results and Systematics

Using the MWPC and the calorimeter reconstructed positions from the data selected in chapter 5, the final calculation of the position resolution, the statistical errors and the study of systematic uncertainties are presented in this chapter.

6.1 Position Resolution

The position resolution of the EMEC to electrons is found by observing the distribution of the difference between the MWPC reconstructed position and the calorimeter reconstruct ed cluster position. In figure 6.1, the distributions of the ϕ position difference for various beam energies is presented. As was previously mentioned in section 5.3, only the Layer 2 of the EMEC is used to calculate the cluster position due to its fine ϕ segmentation and good energy deposition. Since the purpose of this work is not finding the angle of the incident particle, the use of all three segments of the calorimeter is not required. The position resolution in ϕ, denoted as σ_ϕ, for each beam energy is given by the width of the narrow peak seen in the distributions presented in figure 6.1. The peak sometimes sits on a broad background due to the uncorrelated events that pass the correlation cut described

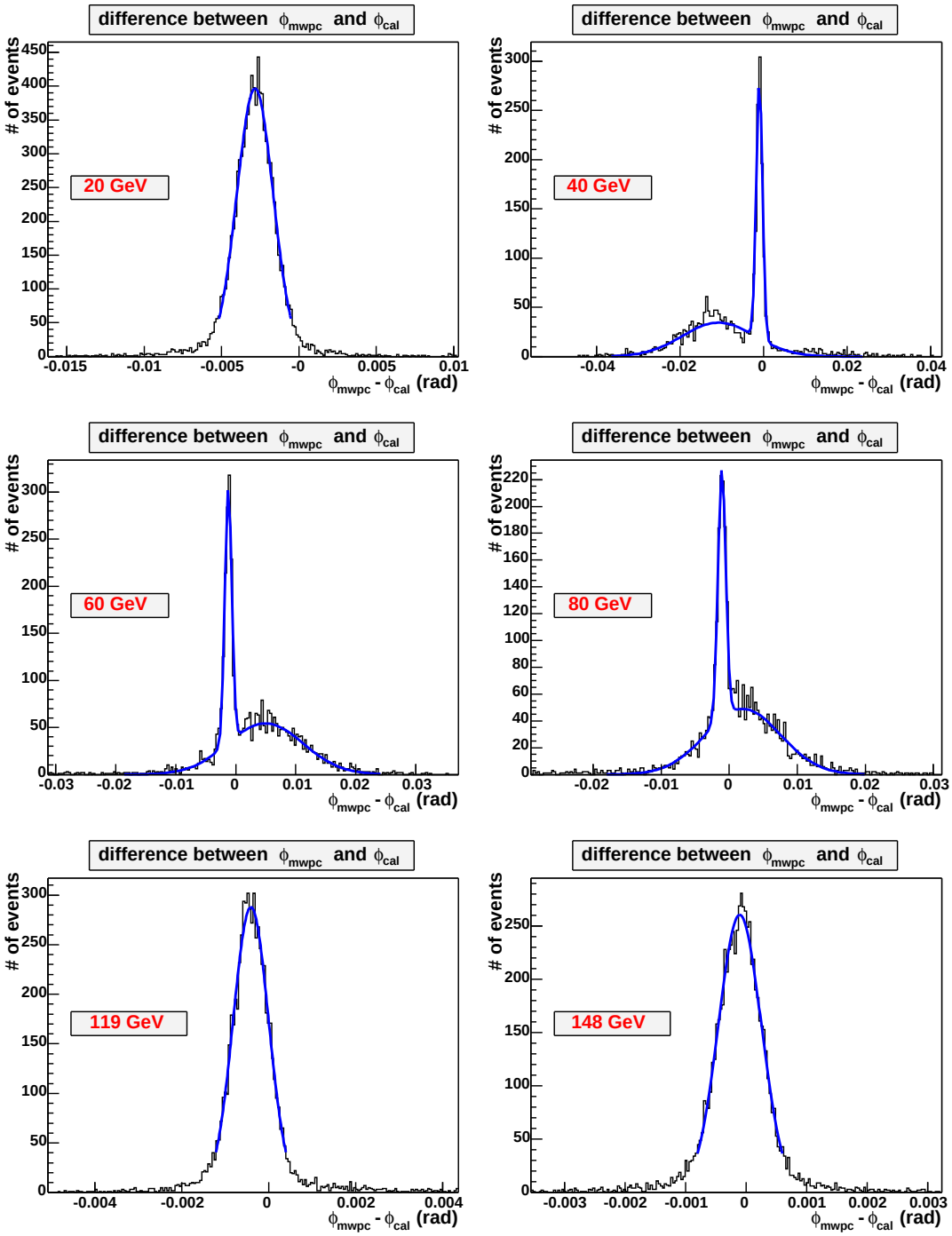

Figure 6.1: The distribution of the difference between ϕ_{mwpc} and ϕ_{cal} for various beam energies in the middle of Layer 2 at impact point J.

in section 5.3. An algorithm (referred to as the resolution extraction algorithm) is applied that uses a fit to extract the ϕ position resolution. The fit is performed using the program MINUIT[32] within ROOT.

The resolution extraction algorithm consists of a fit with a single gaussian or a fit with two gaussians (denoted as a double gaussian). The algorithm starts with an application of a fit with a single gaussian to the distribution of the ϕ position difference over the range, mean$\pm$2rms calculated from the histogram entries. Then, using the mean μ and the error σ from the fit, the distribution is re-fitted with a gaussian in the range $\mu \pm 2\sigma$. This procedure is iterated until the mean of the new gaussian is the same as the previous one. This typically takes only 3-4 iterations. The effect of this is to make the fit range symmetric around the mean. Once the gaussian is symmetric, the goodness (chisquare per degree of freedom, χ^2/ndf) of the fit is checked. If χ^2/ndf is less than 2 (i.e. considered to be good), the algorithm stops and the ϕ position resolution is equal to the sigma of the gaussian. If χ^2/ndf is more than 2, the distribution is assumed to sit on a background that can be approximated with a second gaussian and so the algorithm proceeds with a double gaussian fit. The MINUIT program requires initialization of the parameters of the two gaussians in order for the fitting algorithm to converge on the right peaks (the correlated narrow high peak and the uncorrelated low wide peak). The parameters are initialized with the following values;

$$c_1 = \frac{2}{3} n_{\mathrm{m}} \ , \ \mu_1 = x_{\mathrm{m}} \ , \ \sigma_1 = \frac{\sigma_{\mathrm{h}}}{10}$$
$$c_2 = \frac{c_1}{10} \ , \ \mu_2 = \mu_{\mathrm{h}} \ , \ \sigma_2 = \sigma_{\mathrm{h}}$$

where $c_{1,2}$, $\mu_{1,2}$ and $\sigma_{1,2}$ are the normalization term, the mean and the error of each gaussian, μ_{h} and σ_{h} are the mean and the rms calculated from the data in the the histogram, n_{m}

is the number of events in the highest bin, and $x_{\rm m}$ is the reconstructed position difference value at the center of the highest bin. MINUIT performs the double gaussian fit in the range $\mu_{\rm h} \pm 3\sigma_{\rm h}$ starting with the parameter values given above. The ϕ position resolution is, then, equal to the resulting final value of σ_1. The solid line on each histogram in figure 6.1 corresponds to the result of the fit. The form (single gaussian or double gaussian) of the fit function can clearly be seen and reproduces the data well. The mean χ^2/ndf is about 1.1 for single gaussian and 1.3 for double gaussian.

The ϕ position resolution and the uncertainty calculated using the algorithm above for each impact point and energy is tabulated in appendix D and displayed in figure 6.2. Note that the results from the duplicate runs (see appendix A) at the same energy and impact point are combined by calculating the weighted mean and the associated error. It is obvious from the figure that the position resolution improves as the beam energy increases. This is very much expected since the position is reconstructed using the energy deposition in the calorimeter and the energy resolution improves as the beam energy increases as was discussed in section 2.4.

In order to summarize the performance of the calorimeter independently of the impact point, the weighted means of the resolutions over all of the impact points are calculated at each beam energy. The results are given in table 6.1. The error, $\Delta\sigma_{\phi_{\rm total}}$, on each of these weighted mean resolutions is calculated by adding, in quadrature, the weighted mean error, $\Delta\sigma_{\phi_{\rm stat}}$ (i.e. statistical error), and the uncertainty, $\Delta\sigma_{\phi_{\rm syst}}$, in the resolution due to beam impact position (i.e. the rms of the distribution over all the impact points at each beam energy). The reason for adding the uncertainty due to beam impact position is the

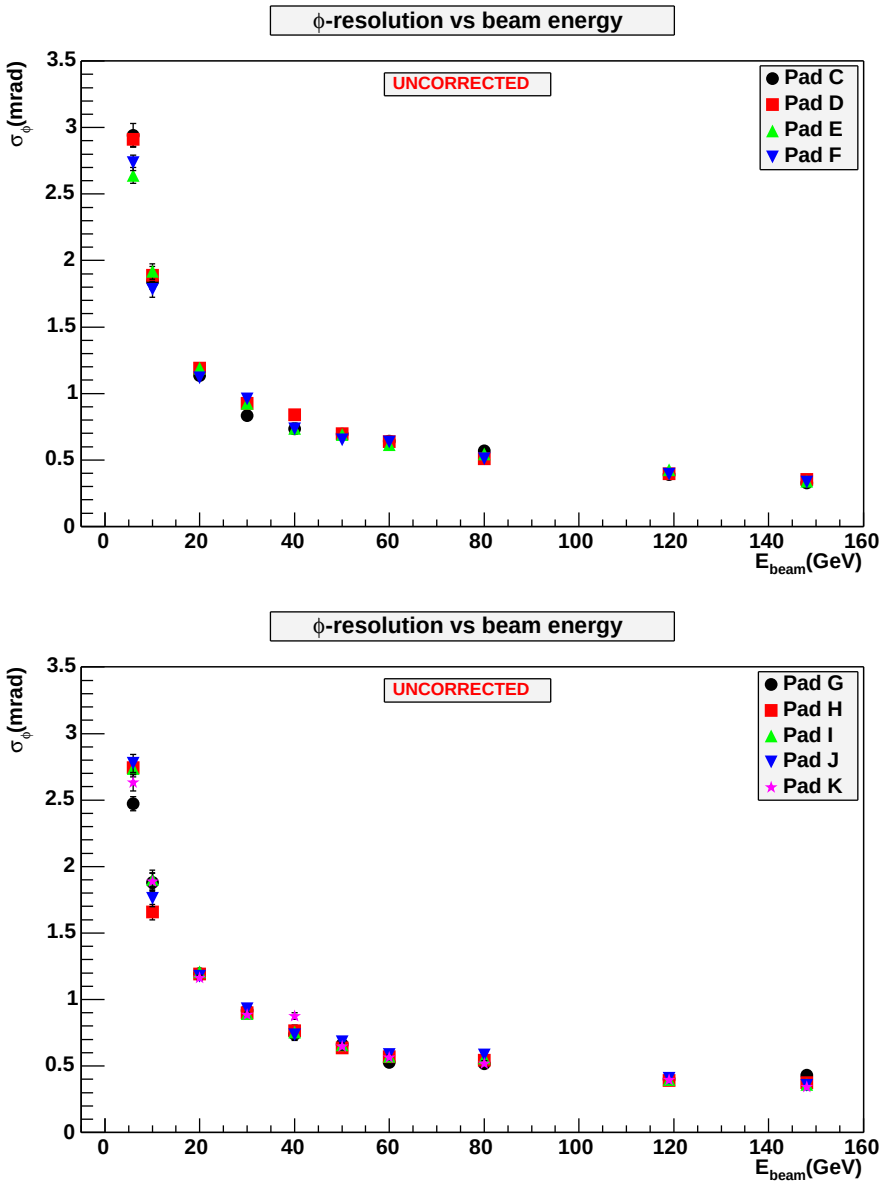

Figure 6.2: The position resolution in ϕ as a function of beam energy for various impact points.

fact that the distribution of the resolution as a function of the beam impact position is too wide to be consistent with the statistical errors at a given energy. This can be observed in figure 6.3 which shows the spatial uniformity of the position resolution. The reason for the

E_{beam} (GeV)	σ_ϕ (mrad)	$\Delta\sigma_{\phi_{\text{stat}}}$ (mrad)	$\Delta\sigma_{\phi_{\text{syst}}}$ (mrad)	$\Delta\sigma_{\phi_{\text{total}}}$ (mrad)
6	2.72422	0.020066	0.14331	0.144708
10	1.83304	0.020916	0.0858747	0.0883853
20	1.17635	0.005536	0.0307132	0.0312081
30	0.907633	0.006214	0.0351956	0.0357399
40	0.771259	0.008976	0.0528185	0.0535758
50	0.669754	0.008071	0.022695	0.0240873
60	0.599008	0.006287	0.0401868	0.0406756
80	0.536948	0.006671	0.0271594	0.0279666
119	0.397448	0.001653	0.011564	0.0116816
148	0.355515	0.001685	0.0316453	0.0316901

Table 6.1: Weighted means and their uncertainties of the uncorrected position resolution results for 6-148 GeV electrons independent of the impact point.

variation is not understood. At a given energy, each point corresponds to a different beam impact position and the error bar plotted is the statistical error on the resolution. These mean resolutions are plotted in figure 6.4.

The data are fit with a function of the beam energy [33] given by

$$\sigma_\phi = \frac{a}{\sqrt{E}} \oplus \frac{b}{E} \oplus c \tag{6.1}$$

where E is the incident beam energy in GeV, and the three terms are the sampling, the noise and the local constant term. The form of the function is the same as the energy resolution formula 2.12 because the precision of the reconstructed position (see formula 5.1) depends mainly on the energy response of the calorimeter. The position resolution of the EMEC in ϕ is found to be $(4.33 \pm 0.10)/\sqrt{E} \oplus (12.77 \pm 0.89)/E \oplus (0.00 \pm 0.10)$ in milliradians. The χ^2/ndf, the ndf and the probability of the fit is 0.404, 7 and 90% respectively.

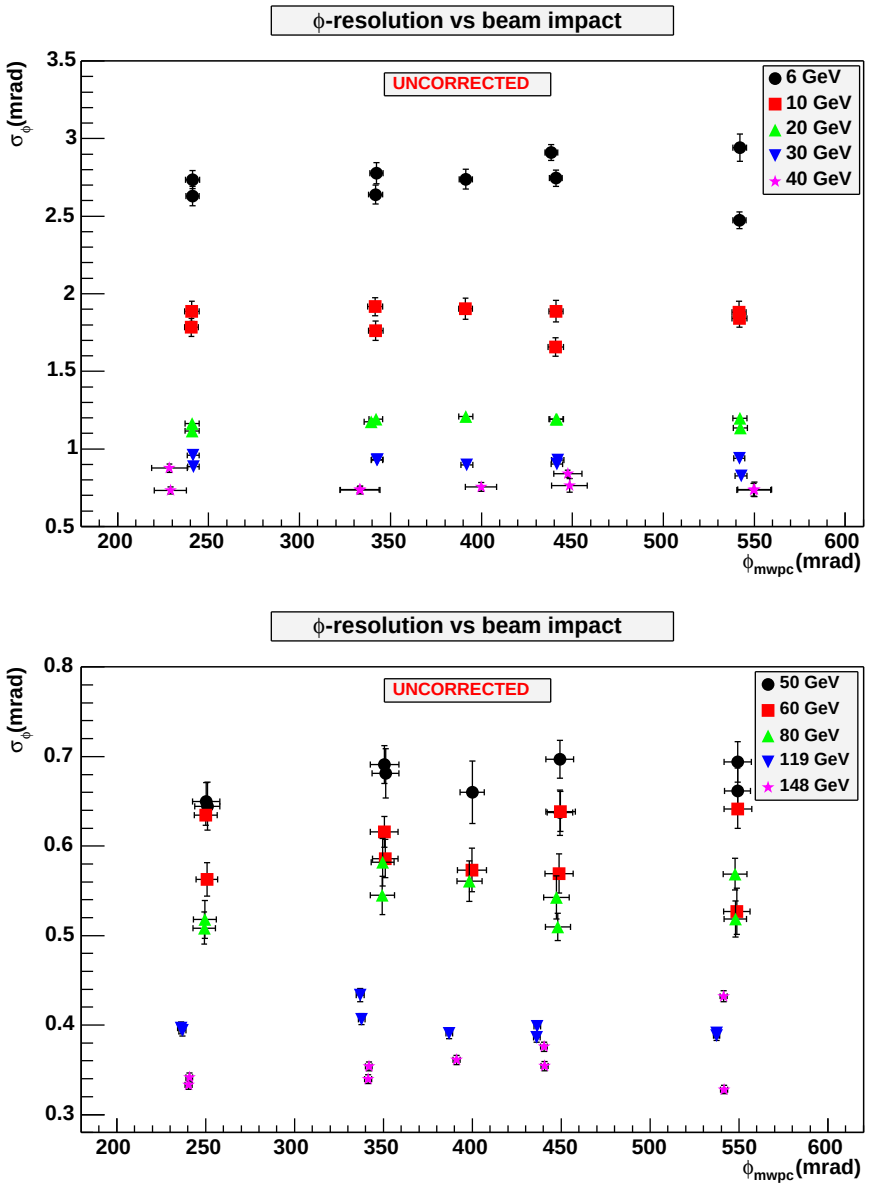

Figure 6.3: The position resolution in ϕ as a function of beam impact position.

6.2 Corrections

The accordion structure of the EMEC introduces small periodic variations in energy response as a function of ϕ, known as *ϕ-modulation* [34]. This periodic modulation can be

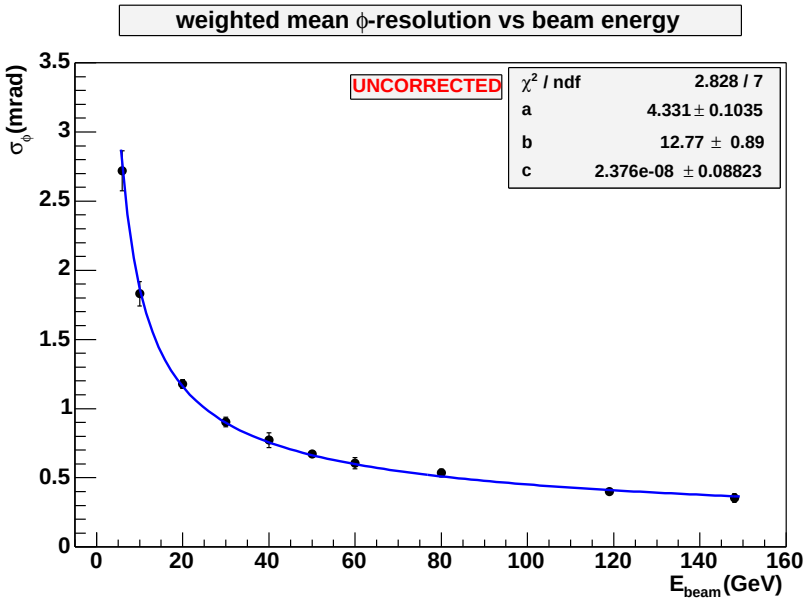

Figure 6.4: The mean position resolution in ϕ as a function beam energy independent of the beam impact.

demonstrated by plotting the normalized energy response of 119 GeV electrons as a function of ϕ in cell units as shown in the upper plot in figure 6.5. The observed ϕ-modulation is due to the sum of two effects: non-uniformity of the sampling fraction near the accordion folds, and non-uniformity of the electric field between the absorber and the electrode folds. The effect of non-uniformity of the sampling fraction near the absorber fold can be understood by considering an essentially non-interacting particle like muon passing through the calorimeter. Since the accordion folds are not perfectly sharp, the muon traverses more LAr near the end of the accordion folds. Therefore, the calorimeter response is enhanced when a particle is incident in a region of a cell where the end of one of the accordion folds is located. The enhancement is bigger near the absorber fold because it is thicker than the electrode fold. Therefore, in figure 6.5, one sees from these two effects that there are two

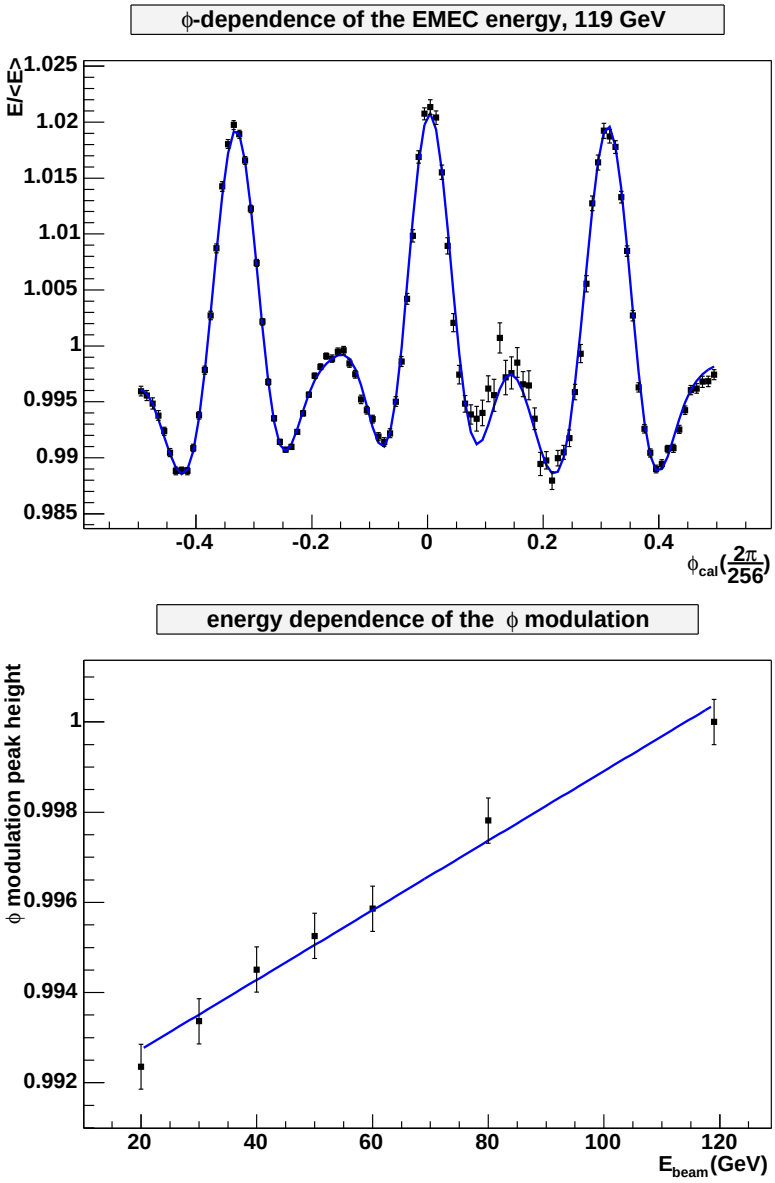

Figure 6.5: The normalized energy response of 119 GeV electrons as a function of ϕ in cell units (upper plot) and the energy dependence of the ϕ modulation (lower plot). The lower plot shows the ϕ modulation peak height (normalized to 119 GeV) as a function of beam energy.

sets of peaks with different amplitudes at the positions of the absorber and the electrode folds corresponding to the three-fold structure of a readout cell in layer 2. There are 768

absorbers in the EMEC outer wheel and the ϕ size of a cell in layer 2 is $2\pi/256$. Hence, there are 3 absorbers per readout cell in layer 2. The variation in response due the accordion structure is parametrized with an adhoc function of the form

$$f(\phi_{\text{fold}}) = a_0 + \sum_{i=1}^{3} [b_i \cos(c_i \phi_{\text{fold}} - d_i) + m_i \sin(n_i \phi_{\text{fold}} + s_i)] \quad . \tag{6.2}$$

There is a very small incident beam energy dependence seen in the lower plot in figure 6.5 that is parametrized by a first degree polynomial, $f(E_{\text{beam}})$. This variation is corrected for on an event by event basis by multiplying the energy response of cluster cells that are in the same ϕ slice as the seed cell with $1/[f(\phi_{\text{fold}}) \times f(E_{\text{beam}})]$. The reason for correcting only the center ϕ slice of the cluster is that the modulation is mainly going to be caused by the particles at the shower center since the particles away from the shower axis traverse the detector at wide angles. The rms of the energy response modulation after correction is less than 0.4%. The effect of this correction on the position resolution is studied by reproducing figure 6.4 and found to be minimal (within the errors e.g. $a = 4.38 \pm 0.11$).

The energy response uniformity in ϕ from cell to cell is studied as well. In order to study the energy response uniformity, the calculated cluster energy normalized to the mean value for a given run is entered into a 2-dimensional histogram as a function of the cluster position for each event for all the selected data. The result is that the data practically scans the calorimeter in the ϕ direction. The histogram is initially binned along the x-axis (i.e cluster position) such that the width of each bin corresponds to the size of a cell in ϕ. The normalized energy response as a function of the normalized ϕ slice position over a total of 16 slices of which 4 are empty due to a lack of data are shown in figure 6.6. The figure is known as a profile of the 2-dimensional histogram. Each point and error bar

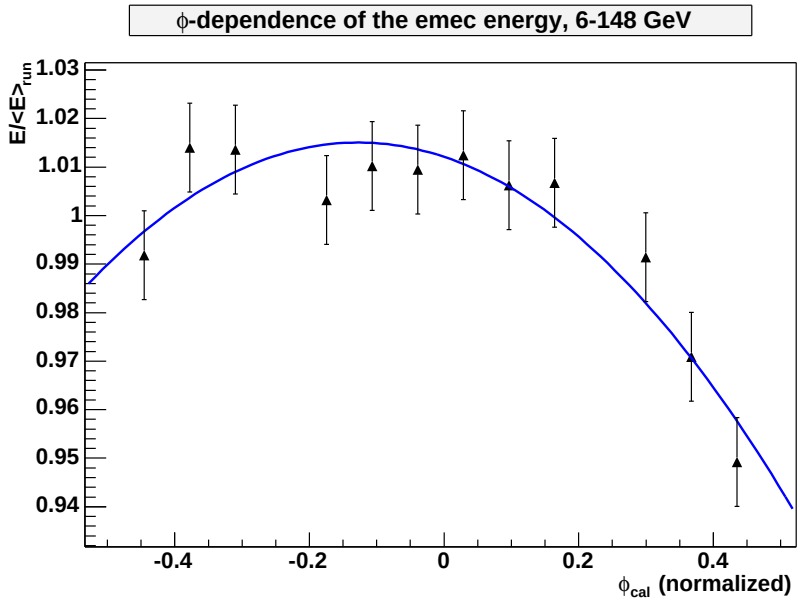

Figure 6.6: The normalized energy response as a function of normalized ϕ slice position. Each point corresponds to a readout channel.

represent the mean energy and the error on the mean calculated from the points in each ϕ slice. The response variation is parametrized with a second degree Legendre polynomial. The correction is applied on an event by event basis. The uniformity corrected position resolution is found to be consistent (i.e. within the errors, in other words no improvement) with the uncorrected results previously obtained.

Another systematic effect, the global cubic time dependence of the calorimeter energy response, is shown in figure 6.7. The figure is produced by a similar procedure to the energy response uniformity. Although, the rms of the variation is about 0.5%, it is parametrized and corrected for on an event by event basis with the sum of a third order polynomial function and a cosine function. The reconstructed position does not change at all with this correction since, for a given event, the same correction factor is applied to all

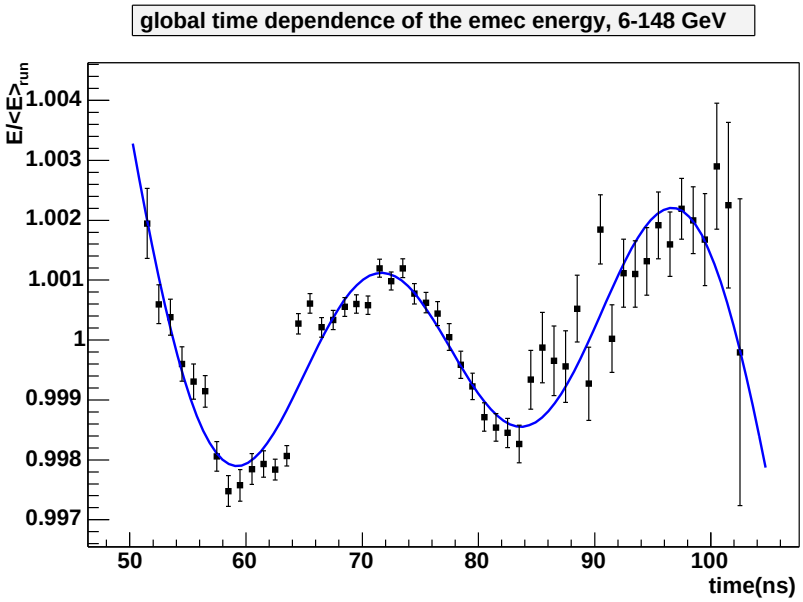

Figure 6.7: The normalized energy response as a function of global time.

cluster cells and hence the factors cancel out (see formula 5.1).

Subsequently, the combined effect of all three corrections on the position resolution is studied. For a given event, the deposited energy in each cluster cell is corrected for the global cubic time dependence and the uniformity in ϕ respectively. Then, the cluster position is calculated and each cluster cell energy is corrected for the ϕ modulation using this cluster position. The resulting corrected ϕ-resolution of the EMEC is found to be

$$\sigma_\phi(\text{mrad}) = \frac{(4.36 \pm 0.10)}{\sqrt{\text{E(GeV)}}} \oplus \frac{(12.64 \pm 0.82)}{\text{E(GeV)}} \oplus (0.00 \pm 0.10) \tag{6.3}$$

as can be seen in figure 6.8.

The effect of the corrections on the position resolutions are found to be negligibly small, although the chisquare per degree of freedom does improve marginally from 2.828/7 to 2.824/7. As an additional check, the corrections are applied in a different order. This

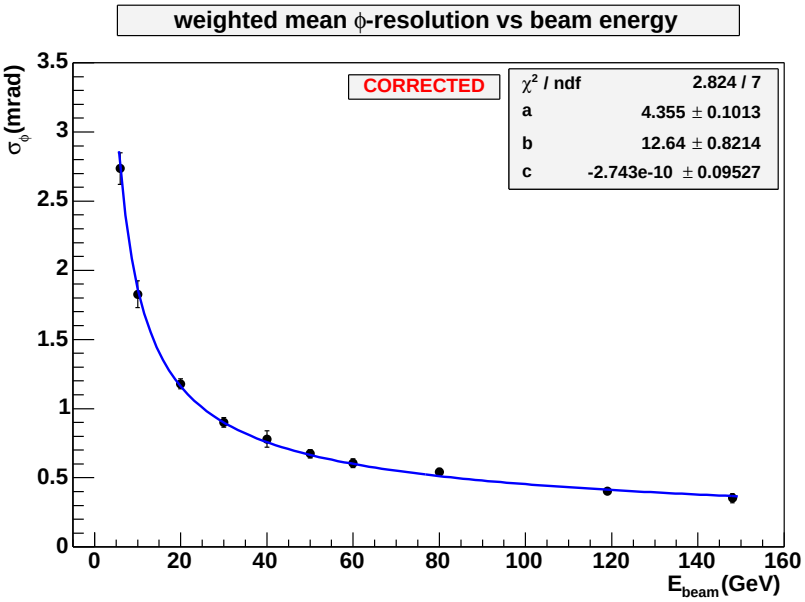

Figure 6.8: The corrected mean position resolution in ϕ as a function beam energy independent of the beam impact.

time, all three corrections are applied after calculating the position with uncorrected data to eliminate the possible degrading effect of the uniformity correction to the ϕ modulation correction in the order explained above. The result of this additional approach turns out to be consistent with the initial corrected result.

In order to ensure the quality of the methods, formulas and the coordinate transformations used in this analysis, various checks are performed. One of these checks is to ensure the suitability of choosing the power n to be unity in the position reconstruction formula 5.1. The effect of the power n on the position resolution is checked for an example 119 GeV run and presented in figure 6.9. It can clearly be noted from the figure that the power unity gives the best ϕ resolution.

Another quality check made is to ensure the accuracy of the transformations be-

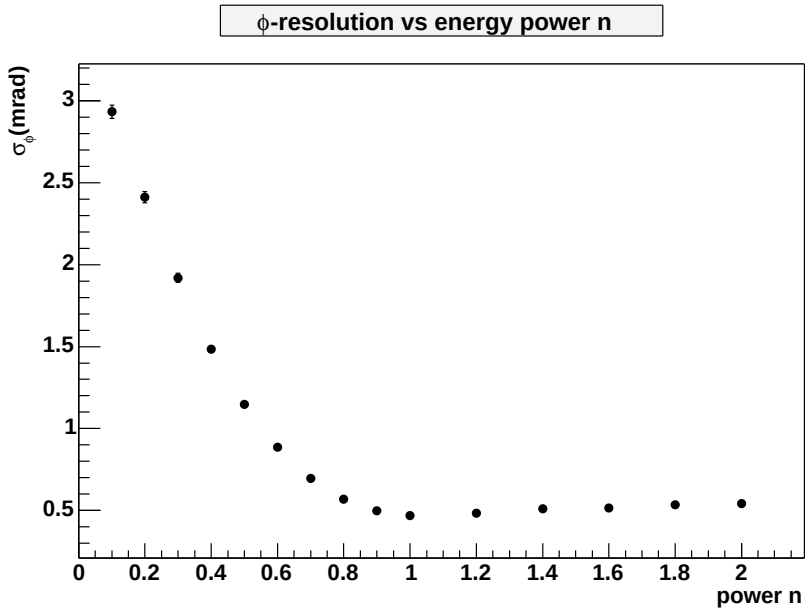

Figure 6.9: The ϕ-resolution as a function of power n in formula 5.1. (update figure in ϕ instead of x)

tween the beam test Cartesian coordinates and the ATLAS coordinates. For this, the mean position difference between the MWPC reconstructed position and the calorimeter reconstructed position is plotted as a function of the MWPC reconstructed beam impact position as shown in figure 6.10. One would expect that the distribution of the mean position difference be constant and centered around zero. However, as can clearly be seen, there is a slope and an antisymmetry about zero in the vertical axis. The slope is found to be due to an offset of 3.6 cm in x between the beam test and the ATLAS local Cartesian coordinate systems, and the antisymmetry is accounted for a small offset of 0.2 cm in y. Therefore, the offsets x_0 and y_0 in the transformation formula 5.3 were corrected to be $x_0 = -0.2$ cm (i.e. $0 - 0.2$) and $y_0 = 168.2$ cm (i.e. $171.8 - 3.6$) from the nominal values.

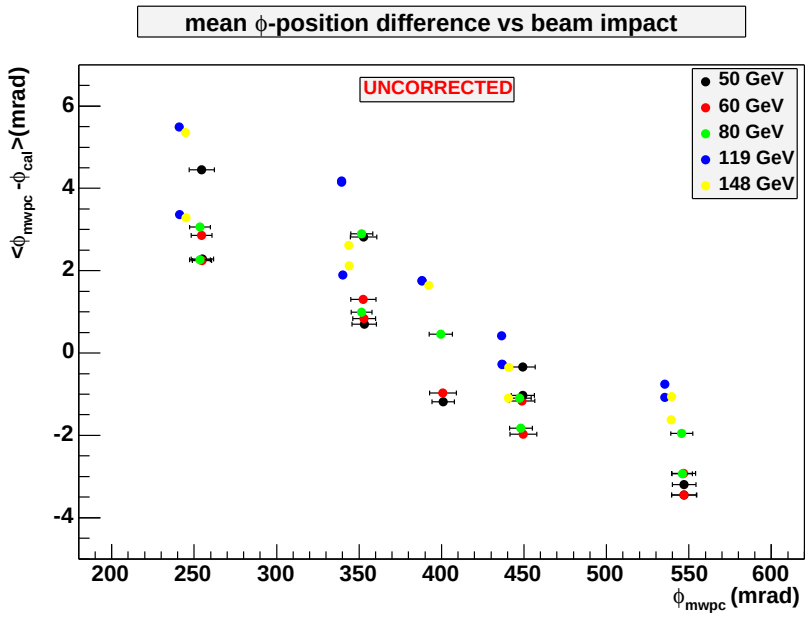

Figure 6.10: Uncorrected mean position difference between the MWPC and the calorimeter reconstructed positions as a function of the beam impact point.

6.3 Alternate Clustering Methods

Two alternative clustering approaches are performed to reconstruct the position and thus assess the ϕ-resolution of the EMEC.

The first of these alternatives is similar to that of the fixed clustering method discussed in Section 5.4. The only difference is that the seed cell is chosen to be the channel with the most deposited energy on an event by event basis instead of a fixed seed cell for an entire run. Therefore, the rectangular area is allowed to move depending on the position of the seed cell for each event. This so called *sliding window clustering* method provides more accurate position information per event. However, when the beam impact point is in the middle of two neighbouring cells, the reconstructed position is a little bit biased towards

the center of one of these neighbouring cells depending on which one is the seed cell in a given event. Due to this small bias, the width of the distribution of the difference between the MWPC reconstructed position and the cluster position is wider, hence the resolution is slightly degraded. Figure 6.11 shows the comparison of the sliding window clustering to the fixed clustering for impact point D as an example and the degradation at 148 GeV is apparent due to the reason discussed above.

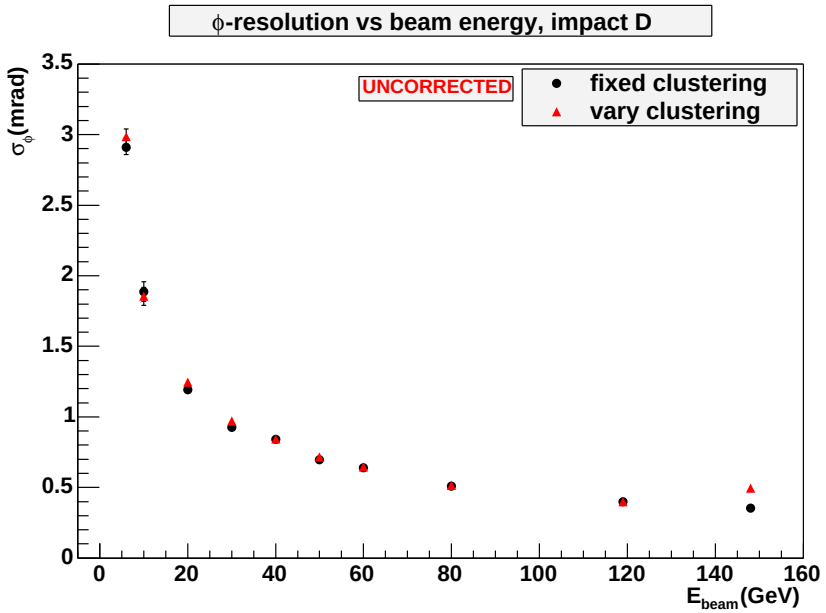

Figure 6.11: The ϕ position resolution as a function of beam energy at impact point D. The figure shows the comparison between the fixed and the sliding window (denoted as vary) clustering methods.

The second clustering approach performed is the rather sophisticated *topological clustering* [25]. In this method, the calorimeter cells are first categorized into two groups: seed cells with deposited energy bigger than $4\sigma_{\text{noise}}$ and neighbor cells with absolute energy bigger than $3\sigma_{\text{noise}}$. Then, one cluster is formed around each seed cell by adding the topo-

logical neighbors with absolute energy bigger than $2\sigma_{\text{noise}}$ and sharing at least one common corner in 2-dimensions with a cell in the neighbor cells group. Finally, the clusters that have one common neighbor cell are merged together. The cluster size obtained for EM showers using this method is bigger than both the fixed and the sliding window clustering techniques. Although, having a bigger cluster size includes more deposited energy and reduces the effect of the beam impact bias introduced by sliding window technique, it also includes more electronics noise which results in the worst position resolution among the three ways of clustering discussed so far. The comparison of this technique to the fixed clustering is shown in figure 6.12. As can be seen from the figure, the topological clustering is better

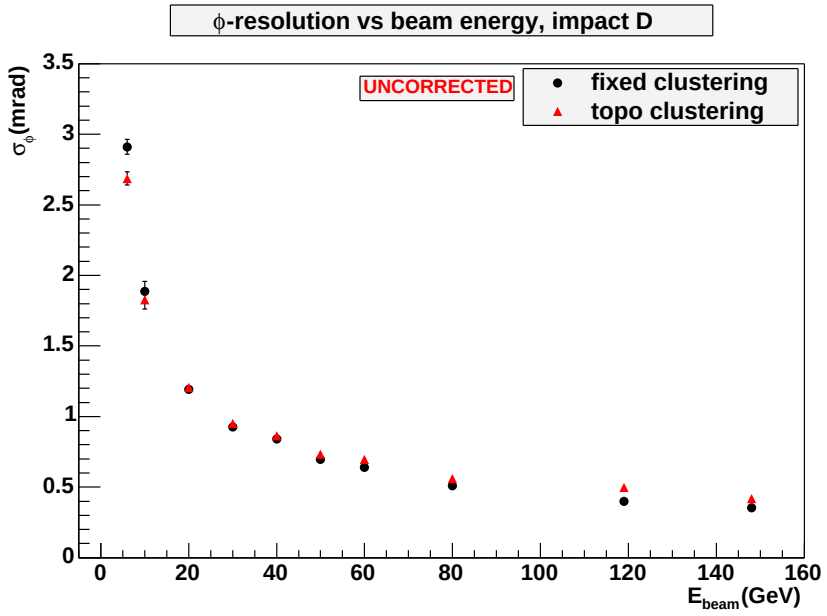

Figure 6.12: The ϕ position resolution as a function of beam energy at impact point D. The figure shows the comparison between the fixed and topological (denoted as topo) clustering methods.

than the fixed clustering method only at 6 GeV and 10 GeV.

Chapter 7

Conclusions

The Electromagnetic Endcap Calorimeter has been designed with a unique accordion structure to provide complete hermiticity and excellent energy and position resolution, attributes on which several physics measurements such as reconstruction of the SM Higgs boson mass will depend.

In the summer of 2002, EMEC and the HEC modules, identical to those installed in the actual ATLAS detector were exposed to beams of electrons, positrons, pions, and muons of energy range 6 GeV $\leq E \leq$ 200 GeV in a beam test using the H6 beam line in the North Area at the CERN SPS. The region studied corresponds to the pseudorapidity interval $1.6 \leq |\eta| \leq 1.8$ in ATLAS. The position reconstruction performance of the EMEC is assessed in terms of its response to electrons in the energy range from 6 GeV to 148 GeV at several impact positions. Unlike the real ATLAS situation, the beam test setup produces a non-pointing geometry in η. Hence, the position resolution of the EMEC is evaluated in the ϕ direction only. Small periodic variations, due to the accordion geometry, in the energy response as a function of ϕ are observed as well as minor time dependent fluctuations and are corrected for. The spatial uniformity of the ϕ-resolution was found to be better than

0.14 mrad at 6 GeV and for energies greater than 6 GeV, it is uniform to 0.09 mrad.

The position resolution of the EMEC in ϕ is measured to be better than

$$\sigma_{\phi_{\rm tot}}({\rm mrad}) = \frac{(4.36 \pm 0.10)}{\sqrt{{\rm E(GeV)}}} \oplus \frac{(12.64 \pm 0.82)}{{\rm E(GeV)}} \oplus (0.00 \pm 0.10) \tag{7.1}$$

where errors of the parameters include the systematic fluctuations with the beam impact position as well as the statistical error. The effect of the MWPC resolution, $\sigma_{\phi_{\rm mwpc}}$, calculated in appendix C can be subtracted and would give

$$\sigma_\phi = \sqrt{\sigma^2_{\phi_{\rm tot}} - \sigma^2_{\phi_{\rm mwpc}}} \tag{7.2}$$

where σ_ϕ is the position resolution of the EMEC. The biggest effect is at high energies where the calorimeter is the most accurate. So for a beam of 119 GeV electrons, the position resolution, $\sigma_{\phi_{\rm tot}}$, of the calorimeter is 0.41 mrad and after subtracting the MWPC contribution, σ_ϕ is 0.37 mrad.

The technical design report [35] gives a value of approximately 7 mrad$\sqrt{\rm GeV}$ as the expectation of the sampling term coefficient. The actual module in the beam test has somewhat better position resolution. Therefore, the modules meet the expectation and are (at energies above 6 GeV) better than what was used to calculate the signal significance for the Higgs in figure 1.7.

References

[1] Griffiths, D. J., *Introduction to Elementary Particles*, John Wiley & Sons Inc., 1987.

[2] Perkins, D. H., *Introduction to High-Energy Physics*, 4^{th} Edition Reprint, Cambridge University Press, 2001.

[3] Halzen, F., Martin, A. D., *Quarks & Leptons: An Introductory Course in Modern Particle Physics*, John Wiley & Sons Inc., 1984.

[4] LHC White Book, CERN/AC/93-03, 1993.

[5] LHC Conceptual Design Report, CERN/AC/95-05, 1995.

[6] The LHC Study Group, *Design Study of the Large Hadron Collider*, CERN/AC/91-03, 1991.

[7] Mellado, B., Unal, G., Wu, S. L., *Higgs Production Cross-Sections and Branching Ratios for the ATLAS Higgs Working Group*, 3 October 2004.

[8] Wielers, M., *Investigation of Higgs Boson in the Low Mass Region with ATLAS*, Lake Louise Talk, Canada, February 2003.

[9] S. Asai et al, *Prospects for the Search for a Standard Model Higgs Boson in ATLAS using Vector Boson Fusion*, arXiv:hep-ph/0402254, 24 February 2004.

[10] Particle Data Group, *Review of Particle Physics*, Physical Review D Particles and Fields, Volume 66, American Physical Society, 2002.

[11] Wigmans, R., *Energy Measurement in Particle Physics*, Calorimetry, Oxford Clarendon Press, 2000.

[12] Grupen C., Böhrer A., Luděk S., *Particle Detectors*, Cambridge Monographs on Particle Physics Nuclear Physics and Cosmology 5, Cambridge University Press, 1996.

[13] Leo, W. R., *Techniques for Nuclear and Particle Physics Experiments*, Springer-Verlag Berlin Heidelberg, 1987.

[14] W. R. Nelson et al., *Electron-Induced Cascade Showers in Copper and Lead at 1 GeV*, Physical Review, Vol. 149, 1966.

[15] Fernow, R. C., *Introduction to Experimental Particle Physics*, Cambridge University Press, 1986.

[16] Ferbel, T., *Experimental Techniques in High-Energy Physics*, Addison-Wesley, 1985.

[17] Kurchaninov, L., *Modeling of the HEC Electronics Chain*, ATLAS HEC Note 109, 2 March 2001.

[18] ATLAS Technical Proposal for a General Purpose pp Experiment at the Large Hadron Collider at CERN, CERN/LHCC/94-43, 1994.

[19] ATLAS Liquid Argon Calorimeter Technical Design Report, CERN/LHCC/96-41, 1996.

[20] ATLAS Tile Calorimeter Technical Design Report, CERN/LHCC/96-42, 1996.

[21] ATLAS Calorimeter Performance Technical Design Report, CERN/LHCC/96-40, 1996.

[22] C. Bovet et al., *The CEDAR Counters for Particle Identification in the SPS Secondary Beams: A Description and an Operation Manual*, SPS Division, CERN 82-13, 1982.

[23] ATLAS Level-1 Trigger Technical Design Report, CERN/LHCC/98-014, 1998.

[24] Cleland, W. R., Stern E. G., *Signal Processing Consideration for Liquid Ionization Calorimeters in a High Rate Environment*, Nuclear Instruments and Methods, A338 (1994) 467-497.

[25] ATLAS Liquid Argon HEC/EMEC Collaboration, *Hadronic Calibration of the ATLAS Liquid Argon End-Cap Calorimeter in the Pseudorapidity Region* $1.6 \leq |\eta| \leq 1.8$ *in Beam Tests*, Nuclear Instruments and Methods, A531 (2004) 481-514.

[26] ATLAS Collaboration, *ATHENA – The ATLAS Common Framework Developer Guide*, Version 8.0.0, 9 February 2004.

[27] Stroustrup, B., *The C++ Programming Language*, Addison-Wesley, February 2000.

[28] Brun, R., Fons, F., *ROOT – An Object Oriented Data Analysis Framework*, Nuclear Instruments and Methods, A389 (1997) 81-86.

[29] Lefebvre, M., Gable, I., *TBRootAna – User Guide*, Version 0.5, 16 July 2003.

[30] Lefebvre, M., Private communication.

[31] Goldstein, H., *Classical Mechanics*, Addison-Wesley, 1980.

[32] James, F., *MINUIT – Function Minimization and Error Analysis Reference Manual*, Version 94.1, August 1998.

[33] B. Aubert et al, *Performance of an Endcap Prototype of the ATLAS Accordion Electromagnetic Calorimeter*, CERN/PPE/96-175, 1996.

[34] Lefebvre M., Parrour G., Pétroff P., *Electromagnetic Liquid Argon Accordion Calorimeter Simulation*, RD3 Note 41, 1993.

[35] ATLAS Detector and Physics Performance Technical Design Report, Volumes I and II, CERN/LHCC/99-14 and 15, 1999.

Appendix A

Beam Test Data Runs

The beam impact point positions are illustrated in figure A.1 and A.2. The list of run numbers which are used in this study of the position resolution of the ATLAS electromagnetic endcap calorimeter is given in table A.1 and A.2. The numbers are only meaningful to the EMEC experts who wish to reproduce the results presented in this work.

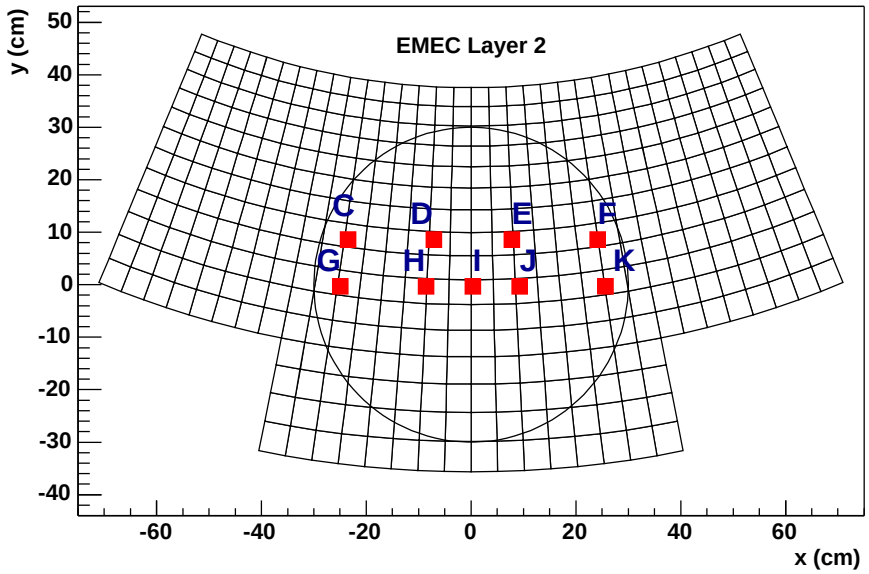

Figure A.1: Standard beam impact point positions projected on the front face of the EMEC layer 2. The large circle is the beam window projection. Horizontal and vertical axes are in the beam test coordinates.

Energy	C	D	E	F	G	H	I	J	K
6	13001	12994	13010	13009	13003	12996	13004	13005	13008
10	12988	12991	12985	12982	12989	12990	12978	12979	12981
20	12921	12922	12951	12974	12920	12918	12976	12953	12975
30	12565 13125	12567 13122	13117	13120	12564 13124	12566 13123	13116	13119	13121
40	12562	12560	12553	12551	12563	12561	12555	12550	12552
50	12544	12541	12538	12537	12543	12542	12547	12549	12536
60	12497	12498	12503	12534	12496	12499	12501	12506	12535
80	12494	12493	12489	12490	12495	12492	12484	12485	12491
119	12707	12704 12705	12691 12692	12690	12708	12706	12686 12687	12688	12689
148	12713	12715	12735	12739	12711	12714	12740	12736	12737

Table A.1: Electron run numbers at standard impact points. Energy is in units of GeV.

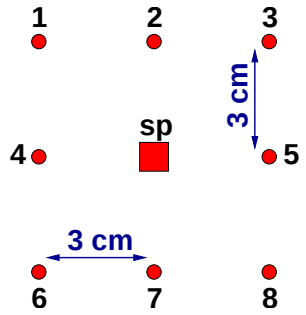

Figure A.2: Positron shape study impact point positions relative to the standard points (sp) illustrated in figure A.1.

Point	C	D	E	F	G	H	I	J	K
sp	12216	12201	12185	12174	12228	12243	12253	12263	12273
1	12221	12203	12189	12176		12237	12249	12261	12268
2	12215	12202	12184	12175		12238	12254	12262	12274
3	12209	12190	12183		12232	12247	12256	12267	12275
4	12219	12205	12188	12177	12223	12236	12250	12260	12269
5	12208	12191	12182	12171	12233	12246	12257	12266	12276
6		12206	12187	12179	12225	12235	12251	12259	12271
7	12217	12248	12186	12173	12227	12244	12252	12264	12272
8		12194	12180	12172	12234	12245	12258	12265	12277

Table A.2: Positron shape study run numbers at 119 GeV.

Appendix B

Theoretical Shower Shape Analysis

Electromagnetic interactions are the best understood energy-loss mechanisms in high energy physics. Development of an EM shower depends on the density of electrons in the absorber, and is fully explained by QED.

The longitudinal development of the shower can be determined by the radiation length, X_0, which is approximated by [10]

$$X_0 = \frac{716.4A}{Z(Z+1)\ln(287/\sqrt{Z})} \ \frac{\mathrm{g}}{\mathrm{cm}^2} \ \ (\mathrm{Z} > 4) \tag{B.1}$$

where Z and A are the atomic and the mass numbers of the atoms of the medium. The radiation length in a mixture or a compound may be approximated by

$$\frac{1}{X_0} = \sum \frac{w_i}{X_{0i}} \tag{B.2}$$

where w_i and X_{0_i} are the fraction by weight and the radiation length for the i^{th} material.

The lateral development of an electromagnetic shower is described by the Molière radius,R_{M}, which is given as [16]

$$R_{\mathrm{M}} = \frac{21.2 \ \mathrm{MeV}}{\epsilon_{\mathrm{c}}} X_0 \cong 7 \frac{A}{Z} \frac{\mathrm{g}}{\mathrm{cm}^2} \tag{B.3}$$

where ϵ_c is called the critical energy defined as the energy at which the energy loss via bremsstrahlung equals to the energy loss via ionization and is expressed as [14]

$$\epsilon_c \cong \frac{800 \text{ MeV}}{Z + 1.2} \quad . \tag{B.4}$$

On average, 95% of a cascade is contained in a cylinder with radius $2R_M$ ($3.5R_M$ for a 99% containment). The Molière radii of mixtures or compounds of different elements may be calculated by

$$\frac{1}{R_M} = \sum \frac{w_i}{R_{Mi}} = \frac{1}{21.2 \text{ MeV}} \sum \frac{w_i \epsilon_{ci}}{X_{0i}} \tag{B.5}$$

The EMEC consists of absorbers, electrodes and liquid argon(Ar). The absorbers are composed of stainless-steel(assumed iron, Fe), lead(Pb) and glass-fiber prepreg adhesive (assumed Kapton polymide film). The electrodes are three layers of copper(Cu) attached by polymide films. The properties of these materials are shown in Table B.1. To calculate

Material	Thickness (cm)	Z	$\langle Z/A \rangle$	Density (g/cm^3)	X_0 (cm)	R_M (cm)	ϵ_c (MeV)
Fe	0.02	26	0.46556	7.87	1.76	1.69	22
Kapton	0.015 , 0.012		0.51264	1.42	28.6	9.61	
Pb	1.7	82	0.39575	11.35	0.56	1.6	7.4
Ar	0.09 - 0.27	18	0.45059	1.396	14.0	8.0	37
Cu	0.002	29	0.45636	8.96	1.43	9.61	20

Table B.1: The EMEC material properties.

the effective X_0 and R_M of the EMEC in the beam test setup, the volume and the position information of the EMEC outer wheel are needed as well to determine the accordion folding angle, θ, which varies by radius, since the thickness, t_z, of the material crossed by a minimum ionizing particle like muon in the beam test (i.e. 90^o to the front face of the EMEC) is

determined by

$$t_z = \frac{\text{thickness}}{\cos(\theta/2)}. \tag{B.6}$$

Dimensions of the active volume of the EMEC outer wheel is given in Table B.2.

Outer radius	203.4 cm
Inner radius at front face	61.4 cm
Inner radius at rear face	69.9 cm
z position of front face	370.4 cm
z position of rear face	421.4 cm
z length of active volume	51.0 cm

Table B.2: Dimensions of the active volume of the EMEC outer wheel.

The properties of the EMEC outer wheel in terms of its X_0 and $R_{\rm M}$ at any given radius in the beam test setup can now be estimated with information in tables B.1 and B.2. An example of results for radius corresponding to $\eta = 1.6$ is summarized in table B.3. Therefore, 99% of a shower in EMEC is contained in a cylinder with a diameter of 27 cm (7

Radius	156.5 cm
Effective $R_{\rm M}$	3.85 cm
Effective X_0	2.13 cm
Total depth in z	$24X_0$
Depth of Layer 1 in z	$4X_0$
Depth of Layer 2 in z	$16X_0$
Depth of Layer 3 in z	$4X_0$

Table B.3: Effective Molière radius and the radiation length of the EMEC outer wheel at $\eta = 1.6$.

effective $R_{\rm M}$). The size of a cell in layer 2 of EMEC is about 4.26×4.26 cm so that a 7×7 cluster of cells is needed for a 99% containment of the shower energy.

Appendix C

Analytical Calculation of the Position Resolution

The position resolution of EMEC can be estimated analytically by adding, in quadrature, the error on the calorimeter reconstructed position, $\sigma_{\phi_{\rm cal}}$, and the error on the MWPC reconstructed position, $\sigma_{\phi_{\rm mwpc}}$.

The calorimeter reconstructed position in ϕ direction is formulated as

$$\phi_{\rm cal} = \frac{\sum\limits_i \phi_i E_i}{\sum\limits_i E_i} \tag{C.1}$$

where ϕ_i and E_i are the barycenter position and the deposited energy of $i^{\rm th}$ channel in the cluster of a given longitudinal segment, respectively. The barycenter position of each EMEC channel is precisely known. Therefore, the error on $\phi_{\rm cal}$ is due to the energy resolution of EMEC only. Using the error propagation theory, the variance of $\phi_{\rm cal}$ is given by

$$\sigma^2_{\phi_{\rm cal}} = \sum_i \left[\sigma^2_{E_i} \left(\frac{\partial \phi_{\rm cal}}{\partial E_i} \right)^2 + \sum_{j \neq i} {\rm cov}(E_i, E_j) \left(\frac{\partial \phi_{\rm cal}}{\partial E_i} \right) \left(\frac{\partial \phi_{\rm cal}}{\partial E_j} \right) \right]. \tag{C.2}$$

A 119 GeV electron run at impact point K is considered as an example. For simplicity, a 3x3 cluster in Layer 2 of EMEC is formed around the seed cell (i.e. the maximum energy deposited channel), and each ϕ slice is assumed as one channel, resulting in three

tall adjacent channels along ϕ. Hence, i and j in equation C.2 run from 1 to 3. The mean deposited energy is determined for each of these channels and the error, σ_{E_i} is calculated with the knowledge of the energy resolution which is found [25] to be

$$\frac{\sigma(E)}{E} = \frac{12.1\%\sqrt{\text{GeV}}}{\sqrt{E}} \oplus 0.4\% \tag{C.3}$$

with $\alpha_{em} = 0.43$ MeV/nA. The covariances of these energies are approximated by evaluating the three channels in the middle η row of the cluster. The values obtained for each parameter on the right hand side of equation C.2 is presented in table C.1. Substitution of these

Parameter	Value
$< E_1 >$	(19.48 ± 0.54) GeV
$< E_2 >$	(65.79 ± 1.02) GeV
$< E_3 >$	(4.04 ± 0.24) GeV
cov(E_1,E_2)	-1.80 $(\text{GeV})^2$
cov(E_1,E_3)	-0.75 $(\text{GeV})^2$
cov(E_2,E_3)	0.62 $(\text{GeV})^2$

Table C.1: Input parameters of equation C.2.

values in equation C.2 yields an error of $\sigma_{\phi_{\text{cal}}} = 0.43$ mrad on the calorimeter reconstructed position.

The MWPC reconstructed x-position in a given depth z in the beam test coordinates is expressed as

$$x_{\text{mwpc}} = x_0 + x_1 z \tag{C.4}$$

where x_0 is the intercept and x_1 is the slope calculated by the least squares fit performed on the position information provided by the MWPCs. By propagation of errors, the variance of x_{mwpc} is derived to be

$$\sigma^2_{x_{\text{mwpc}}} = \sigma^2_{x_0} + z^2\sigma^2_{x_1} + 2z\text{cov}(x_0, x_1). \tag{C.5}$$

The error terms in equation C.5 are available in the ATHENA output ROOT file for a given run for each event (see section 5.1). The values for an example event from the 119 GeV run at impact point K is shown in table C.2 along with the z-distance from the barycenter position of the seed cell to $z = 0$. Substitution of these values in equation C.5

Parameter	Value
$\sigma^2_{x_0}$	1.09×10^{-3} (cm)^2
$\sigma^2_{x_1}$	1.35×10^{-9} (cm)^2
cov(x_0,x_1)	6.57×10^{-7} (cm)^2
z	97.86 cm

Table C.2: Input parameters of equation C.5.

yields an uncertainty of $\sigma_{x_{\mathrm{mwpc}}} = 312$ μm on the MWPC reconstructed position in the beam test coordinate system. The size of the seed cell is 4.26 cm in x of the beam coordinates and 0.0245 rad in ϕ of the ATLAS coordinates. Hence, the error on the MWPC reconstructed position can be converted to ATLAS coordinate system and found as $\sigma_{\phi_{\mathrm{mwpc}}} = 0.18$ mrad. Note that the half width of the cluster of the MWPC wires hit is used to calculate the errors on the fit parameters, so the errors are over estimated and hence $\sigma_{\phi_{\mathrm{mwpc}}}$ is likely to be over estimated as well.

As a result, the ϕ resolution of the EMEC is estimated to be

$$\sigma_\phi = \sigma_{\phi_{\mathrm{cal}}} \oplus \sigma_{\phi_{\mathrm{mwpc}}} = 0.47 \text{ mrad} \tag{C.6}$$

for 119 GeV electrons at impact point K which is close to the measured value of 0.41 mrad.

Appendix D

Summary of Position Resolution Results

Point	E_{beam} (GeV)	σ_ϕ (mrad)	$\Delta\sigma_\phi$ (mrad)	E_{beam} (GeV)	σ_ϕ (mrad)	$\Delta\sigma_\phi$ (mrad)
C	6	2.9416	0.089088	20	1.13516	0.0182855
D	6	2.9106	0.0521731	20	1.1923	0.0165628
E	6	2.63951	0.0596333	20	1.19171	0.0142302
F	6	2.73525	0.058524	20	1.11657	0.0207536
G	6	2.47247	0.0539493	20	1.19619	0.0159451
H	6	2.74496	0.0528855	20	1.19132	0.0166772
I	6	2.73854	0.0643733	20	1.20855	0.0180455
J	6	2.77679	0.0677968	20	1.17466	0.0142705
K	6	2.63034	0.0624284	20	1.16368	0.0176003
C	10	1.84217	0.058326	30	0.834947	0.0155733
D	10	1.88781	0.0687483	30	0.926606	0.0185087
E	10	1.91728	0.0581864	30	0.926799	0.0236583
F	10	1.7837	0.058811	30	0.95782	0.0212211
G	10	1.88121	0.0696714	30	0.918773	0.0165311
H	10	1.65682	0.0593756	30	0.901706	0.0151706
I	10	1.90352	0.0677713	30	0.895644	0.0255227
J	10	1.76092	0.0627379	30	0.932131	0.0221889
K	10	1.88687	0.0653334	30	0.885467	0.017459

Table D.1: Uncorrected position resolution results from 6 to 30 GeV electrons.

Point	E_{beam} (GeV)	σ_ϕ (mrad)	$\Delta\sigma_\phi$ (mrad)	E_{beam} (GeV)	σ_ϕ (mrad)	$\Delta\sigma_\phi$ (mrad)
C	40	0.735767	0.0408176	80	0.568683	0.0176762
D	40	0.84118	0.0223899	80	0.509702	0.0154495
E	40	0.736598	0.0196082	80	0.545028	0.0214212
F	40	0.732869	0.0221435	80	0.508418	0.0180576
G	40	0.738783	0.0466451	80	0.518564	0.0200022
H	40	0.764741	0.0428299	80	0.542463	0.0240055
I	40	0.754946	0.0288492	80	0.560792	0.0223942
J	40	0.735305	0.0260588	80	0.581975	0.0267268
K	40	0.875712	0.0258444	80	0.518037	0.0212709
C	50	0.693909	0.0226305	119	0.389431	0.00519632
D	50	0.696829	0.0210615	119	0.396751	0.00413576
E	50	0.690997	0.0212231	119	0.427523	0.00550034
F	50	0.649989	0.0207769	119	0.394379	0.00575508
G	50	0.661441	0.0255937	119	0.40234	0.00528028
H	50	0.637306	0.025492	119	0.391204	0.00499771
I	50	0.660213	0.0349849	119	0.398707	0.00395943
J	50	0.681132	0.0275494	119	0.407329	0.00540954
K	50	0.644574	0.0266386	119	0.39539	0.00549129
C	60	0.641283	0.021707	148	0.327846	0.00470158
D	60	0.63865	0.0224803	148	0.35423	0.00522835
E	60	0.615786	0.0173109	148	0.339394	0.0049301
F	60	0.634634	0.011547	148	0.333136	0.00476295
G	60	0.527048	0.0258249	148	0.432258	0.00633279
H	60	0.569251	0.0219523	148	0.375793	0.00503891
I	60	0.573225	0.0242299	148	0.36109	0.0051687
J	60	0.585951	0.0213532	148	0.353868	0.00483557
K	60	0.56279	0.0185949	148	0.341664	0.00498111

Table D.2: Uncorrected position resolution results from 40 and 148 GeV electrons.

University of Victoria
Partial Copyright License

Title of Thesis:

Position Resolution of the ATLAS Electromagnetic Endcap Calorimeter

Author: _____

Tayfun Ince

Signed: June 1, 2005